MASARYKOVA
UNIVERZITA

PŘÍRODOVĚDECKÁ FAKULTA

Analýza gravitačních vln ze splynutí kompaktních složek binárních systémů

Diplomová práce

LEONTÝNA HERGETOVÁ

Brno, jaro 2026

MASARYKOVA
UNIVERZITA

PŘÍRODOVĚDECKÁ FAKULTA

Analýza gravitačních vln ze splynutí kompaktních složek binárních systémů

Diplomová práce

LEONTÝNA HERGETOVÁ

Vedoucí práce: Mgr. Ing. arch. Petr Kurfürst, Ph.D.

Ústav teoretické fyziky a astrofyziky

Brno, jaro 2026

MUNI
PŘÍRODOVĚDECKÁ
FAKULTA

Bibliografický záznam

Autor:	Leontýna Hergetová Přírodovědecká fakulta Masarykova univerzita Ústav teoretické fyziky a astrofyziky

Název práce:	Analýza gravitačních vln ze splynutí kompaktních složek binárních systémů
Studijní program:	Fyzika
Obor:	Teoretická fyzika
Vedoucí práce:	Mgr. Ing. arch. Petr Kurfürst, Ph.D.
Akademický rok:	2025/2026
Počet stran:	xiv + 95
Klíčová slova:	Gravitační vlny, Odhad parametrů, Splynutí kompaktních složek binárních systémů, Effective One Body formalismus, Diferenciální evoluce, Chirp mass, PyCBC

Bibliographic record

Author:	Leontýna Hergetová Faculty of Science Masaryk University Department of Theoretical Physics and Astrophysics

Title of Thesis:	Analysis of gravitational waves from compact binary mergers
Degree Programme:	Physics
Field of Study:	Theoretical physics
Supervisor:	Mgr. Ing. arch. Petr Kurfürst, Ph.D.
Academic Year:	2025/2026
Number of Pages:	xiv + 95
Keywords:	Gravitational Waves, Parameter Estimation, Compact Binary mergers, Effective One-Body Formalism, Differential Evolution, Chirp Mass, PyCBC

Abstrakt

Od prvního objevu v září 2015 se detekce gravitačních vln za posledních 11 let stala rychle se rozvíjejícím oborem, který vedl k zdokonalení technik analýzy dat. Tato práce analyzuje čtyři zajímavé detekce gravitačních vln s cílem odhadnout počáteční hmotnosti složek binárnách systémů a chirp mass. Tato analýza byla provedena modelováním dat získaných prostřednictvím PyCBC s využitím Effective One-Body(EOB) formalismu v kombinaci s algoritmy diferenciální evoluce (DE) pro odhad parametrů. Výsledky ukazují, že tento přístup založený na DE může poskytnout odhady hmotnosti, které jsou v souladu s odhady odvozenými pomocí tradičních modelovacích strategií v publikované literatuře, což potvrzuje jeho účinnost při analýze dat gravitačních vln.

Abstract

Since the first observation in September 2015, the detection of gravitational waves has become a fast-evolving field of research over the last 11 years, driving improvements in data analysis techniques. This thesis analyses four interesting gravitational wave detections to estimate the initial component masses of the binary systems and the chirp mass. This analysis was conducted by modelling data acquired via PyCBC using the Effective One-Body (EOB) formalism, combined with differential evolution (DE) algorithms for parameter estimation. The results demonstrate that this DE-based approach could yield mass estimates consistent with those derived using traditional modelling strategies in published literature, validating its effectiveness in gravitational waves' data analysis.

MUNI
SCI

MASARYKOVA UNIVERZITA
PŘÍRODOVĚDECKÁ FAKULTA
KOTLÁŘSKÁ 2, 611 37 BRNO
IČ: 00216224
DIČ: CZ00216224

ZADÁNÍ DIPLOMOVÉ PRÁCE

Akademický rok: 2024/2025

Ústav:	Ústav teoretické fyziky a astrofyziky
Studentka:	Bc. Leontýna Hergetová
Program:	Fyzika
Specializace:	Teoretická fyzika

Ředitel *ústavu* PřF MU Vám ve smyslu Studijního a zkušebního řádu MU určuje diplomovou práci s názvem:

Název práce:	Analýza gravitačních vln ze splynutí kompaktních složek binárních systémů
Název práce anglicky:	Analysis of gravitational waves from compact binary mergers
Jazyk práce:	angličtina

Oficiální zadání:
This thesis will develop the previous topic of the bachelor thesis ”Gravitational waves: a new window to the universe”. Catastrophic events, in particular the merger of two compact objects, i.e. black holes or neutron stars, or combinations thereof, lead to detectable gravitational wave emissions and represent the most energetic processes in the Universe. They can also in some cases be identified with the source of electromagnetic radiation, allowing their precise localization and observational confirmation of other essential characteristics. This thesis will analyse these events in more detail, study gravitational wave theory in much greater detail than the above bachelor thesis, i.e. ”from scratch”, attempt to determine the masses of the individual components of the original binary, not just the total mass, and also fit measured data from gravitational wave detectors in an advanced way.

Literatura:
WALD, Robert M. *General relativity*. Chicago: The University of Chicago, 1984, xiii, 491. ISBN 0226870332.

MISNER, Charles W., Kip S. THORNE a John Archibald WHEELER. *Gravitation*. San Francisco: W.H. Freeman and Company, 1973, xxvi, 1279. ISBN 0716703343.

Gravitational-wave physics and astronomyan introduction to theory, experiment and data analysis. Edited by Jolien D. E. Creighton - Warren G. Anderson. Weinheim, Germany: Wiley-VCH, 2011, xiv, 375 p. ISBN 9783527636051.

Vedoucí práce:	Mgr. Ing. arch. Petr Kurfürst, Ph.D.
Konzultant:	RNDr. Michal Zajaček, Dr. rer. nat.
Datum zadání práce:	25. 7. 2024
V Brně dne:	6. 5. 2025

Zadání bylo schváleno prostřednictvím IS MU.

Bc. Leontýna Hergetová, 3. 9. 2024
Mgr. Ing. arch. Petr Kurfürst, Ph.D., 18. 10. 2024
Mgr. Dušan Hemzal, Ph.D., 27. 11. 2024

Poděkování

V první řadě bych chtěla poděkovat svému vedoucímu Mgr. Ing. arch. Petru Kurfürstovi, Ph.D., který mou práci vedl i přes specializaci v jiné oblasti výzkumu. Dále bych chtěla poděkovat doc. RNDr. Michalu Zajačkovi, Dr. rer. nat., který mi napomohl dostat se do centra dění a prohloubit vztahy s kolegy z oboru. Také bych chtěla poděkovat spolužákům, se kterými jsem přežila studium. V neposlední řadě musím poděkovat svým ženám, které mě dokázaly rozesmát a podržet vždy, když bylo třeba, a své rodině, především mamce, která tu se mnou vždycky byla. Děkuji, že jste mi nablízku, i když jsme od sebe půl republiky daleko.

Prohlášení

Prohlašuji, že jsem svoji diplomovou práci vypracovala samostatně pod vedením vedoucího práce s využitím informačních zdrojů, které jsou v práci citovány.

Leontýna Hergetová

Contents

Introduction **1**

I Theoretical section **3**

1 Linear theory in a weak field approximation **5**
1.1 Equation of motion 5
1.2 The Lorentz gauge condition 6
1.3 The metric 10
1.4 Application of the weak-field limit to gravitational radiation 11

2 Polarisation of gravitational waves **14**

3 Gravitational waves emitted from a two-body system **17**
3.1 Energy of the gravitational waves 17
3.2 Important parameters of emitted gravitational waves . 25

II Analytical section **34**

4 Introduction to signal processing **36**
4.1 PyCBC 36
4.1.1 Installation process 36
4.2 Used waveform 37
4.2.1 Effective one-body waveform (EOB) 37
4.2.2 Used models 40
4.3 Optimisation 41
4.3.1 Differential Evolution (DE) 41

5 GW150814 **44**
5.1 Data preparation 44
5.1.1 Whitening 45
5.1.2 Bandpassing 46
5.2 Modelling of the data 48

5.2.1 Match Function 48
5.2.2 Optimisation 49
5.2.3 Final assembly 50
5.3 Additional information on data and chirp mass calculation 52
5.4 Results 53

6 GW170814 **54**
6.1 Data preparation 54
6.2 Modelling of the data 56
6.3 Results 58

7 GW170817 **60**
7.1 Data preparation 60
7.2 Modelling of the data 62
7.3 Results 64

8 GW231123 **65**
8.1 Data preparation 65
8.2 Modelling of the data 67
8.3 Results 71

9 Overall results of analysis **72**

10 Conclusion **73**

References **76**

Index **79**

A Appendix **80**
A.1 Detailed calculations from chapter "Linear theory in weak field approximation" 80
A.1.1 Equation of linearised gravity using trace-reversed tensor (1.13) 80
A.1.2 Derivatives used for coordinate change (1.16) . 80
A.1.3 Trace reversed perturbation with gauge condition (1.18) 81

A.2 Detailed calculations from chapter "Gravitational waves emitted from a two-body system" 82
A.2.1 Calculation of the last non-linear term in the second-order Ricci tensor (3.3) 82
A.2.2 Verification of tracelessness and transversality of $q^{ij}_{TT} = Q^{ij}_{TT}$ 83
A.2.3 Calculation of $\partial t_{\text{ret}}/\partial t$ 84
A.2.4 Generalised identities for the solutions of Equation (3.33) 85
A.3 The complete code for the numerical analysis 86
A.3.1 The exemplary code for the H1 of GW150914. . 86
A.3.2 The snippet for L1 of GW150914 92

List of Tables

5.1 Results of the analysis and modelling of the GW150914 data 53
6.1 Results of the analysis and modelling of the GW170814 data. 59
7.1 Results of the analysis and modelling of the GW170817 data. 64
8.1 Results of the analysis and modelling of the H1 GW231123 data. 71
8.2 Results of the analysis and modelling of the L1 GW231123 data. 71
9.1 Mean values of the final results of each studied event with deviations 72

List of Figures

5.1 Raw GW150814 data. 44
5.2 PSD GW150814 of data. 45
5.3 Whitened PSD of GW150814 data. 46
5.4 Whitened GW150814 data. 46
5.5 Cleaned up GW150814 data. 47
5.6 Zoomed in clean GW150814 data. 48
5.7 *Top:* GW150914 data from Hanford (Washington, US) with optimised model; *Bottom:* Residual signal from modelling GW150914 H1 data. 51
5.8 *Top:* GW150914 data from Livingston (Louisiana, US) with optimised model; *Bottom:* Residual signal from modelling GW150914 L1 data. 52
6.1 Raw GW170814 data. 54
6.2 PDS of GW170814 data before and after whitening. 55
6.3 Clean GW170814 data and their zoom. 56
6.4 *Top:* GW170814 data from Hanford (Washington, US) with optimised model; *Bottom:* Residual signal from modelling GW170814 H1 data. 57
6.5 *Top:* GW170814 data from Livingston (Louisiana, US) with optimised model; *Bottom:* Residual signal from modelling GW170814 L1 data. 58
7.1 Raw GW170817 data. 61
7.2 Zoomed in clean GW170817 data. 61
7.3 PDS of GW170817 data before and after whitening. 62
7.4 *Top:* GW170817 data from Hanford (Washington, US) with optimised model; *Bottom:* Residual signal from modelling GW170817 H1 data. 64
8.1 Raw GW231123 data. 65
8.2 PDS of GW231123 data before and after whitening. 66
8.3 Clean GW231123 data and their zoom. 67

8.4 *First:* GW231123 data from Hanford (Washington, US) with optimised model focused on the inspiral part of the data; *Second:* Residual signal from modelling GW170814 H1 data with focus on the inspiral part; *Third:* GW231123 data from Hanford (Washington, US) with optimised model focused on the merge part of the data; *Fourth:* Residual signal from modelling GW170814 H1 data with focus on the merger part. 69
8.5 *First:* GW231123 data from Livingston (Louisiana, US) with optimised model focused on the inspiral part of the data; *Second:* Residual signal from modelling GW170814 L1 data with focus on the inspiral part; *Third:* GW231123 data from Livingston (Louisiana, US) with optimised model focused on the merge part of the data; *Fourth:* Residual signal from modelling GW170814 L1 data with focus on the merge part. 70

Introduction

First predicted by Albert Einstein in his General Theory of Relativity, gravitational waves were directly observed for the first time in 2015 when two stellar-mass black holes spiralled inward and merged (B. P. Abbott et al. 2016). This historic event proved not only the existence of gravitational waves but also the existence of binary stellar-mass black hole systems. The observation was made possible by the two Advanced LIGO detectors located in the United States.

Since then, the scientific community has continuously worked to improve observational methods through additional terrestrial detectors (both surface and underground) and future space-based observatories, such as the planned LISA mission. However, detection is only the first step. Thorough data analysis and parameter estimation are required to determine the physical properties of the sources that generated these waves.

Parameter estimation provides information about the source system, including initial mass and spin magnitudes, final mass and spin, luminosity distance, and much more. These estimates allow researchers to classify the binary system (such as identifying it as a binary black hole or binary neutron star), determine the mass ratio of the components, including standard, intermediate (IMRI), and extreme mass ratio inspirals (EMRI), and measure how far away the event occurred.

The primary objective of this thesis is to estimate the initial masses and the effective mass, commonly referred to as the chirp mass, for four specific binary merger events. This is achieved by applying a differential evolution (DE) optimisation method to effective one-body (EOB) models, utilising data and frameworks provided by the `PyCBC` package.

This thesis is structured to first provide the theoretical foundation of gravitational wave physics before the numerical and analytical research. The theoretical section introduces the linear theory in the weak-field approximation, where the derivation of the equation of motion, the Lorentz gauge condition, the metric, and polarisation takes place. It also includes a section on the energy and power of gravitational waves emitted by binary systems, which is the primary

focus of the research. Finally, the theoretical section concludes by deriving the key parameters of gravitational waves, including the chirp mass, which is later calculated from the estimated component masses.

The thesis then continues with the analytical section, where the main research is explained and conducted. This begins with an introduction to data processing. Key concepts include the use of `PyCBC` as the primary package for data processing, the EOB formalism on which the models are based, and the specific DE optimisation technique used for parameter estimation. This section ends with four chapters, each dedicated to one of the analysed events.

Finally, the thesis concludes with a summary of the obtained results, the references used, and an appendix containing explanatory calculations and the complete code used for the analysis.

PART I

THEORETICAL SECTION

As is also the case in the preceding bachelor thesis (Hergetová 2024), this work incorporates a section on linear theory in the weak-field approximation. The material in this chapter is primarily based on the work of Michelle Maggiore, as outlined in his publication *Gravitational Waves: Volume 1: Theory and Experiments* (Maggiore 2008), in conjunction with insights from General Relativity (GTR) courses and notes provided by the thesis supervisor.

1 Linear theory in a weak field approximation

1.1 Equation of motion

As is customary in standard linearisation procedures in physics, the goal is to neglect higher-order terms $\mathcal{O}(h_{\mu\nu}^2)$. The most straightforward method of approximation that will result in this is to consider perturbations to be infinitesimal ($|h_{\mu\nu}| \ll 1$), meaning that the Minkowski flat spacetime $\eta_{\mu\nu} = \text{diag}(+1, -1, -1, -1)$ (a fundamental assumption for the Universe) is just slightly deformed. The metric will then assume the following form:

$$g_{\mu\nu} \simeq \eta_{\mu\nu} + h_{\mu\nu} \quad |h_{\mu\nu}| \ll 1. \tag{1.1}$$

The Minkowski flat spacetime is noted $+, -, -, -$, as is more commonly used in quantum field theory instead of the relativistic notation $-, +, +, +$. This choice does not change anything. Physics remains the same, but caution is needed when dealing with positive and negative signs.

It is evident that the metric now contains the deformation (henceforth referred to as LM - linearised metric). The next step is to derive the equation of motion from the Einstein equations of motion in first order(referred to as EFE: Einstein's field equations). Starting with the Christoffel symbols, the known formula is

$$\Gamma_{\mu\nu}^{\rho} = \frac{1}{2} g^{\rho\sigma} (\partial_\nu g_{\sigma\mu} + \partial_\mu g_{\sigma\nu} - \partial_\sigma g_{\mu\nu}); \tag{1.2}$$

changing its form by plugging this into the LM to

$$\Gamma_{\mu\nu}^{\rho} = \frac{1}{2} \eta^{\rho\sigma} \left(\partial_\mu h_{\nu\sigma} + \partial_\nu h_{\mu\sigma} - \partial_\sigma h_{\mu\nu} \right) = \frac{1}{2} \left(\partial_\mu h^{\rho}{}_{\nu} + \partial_\nu h^{\rho}{}_{\mu} - \partial^{\rho} h_{\mu\nu} \right), \tag{1.3}$$

where the $\eta_{\mu\nu}$ derivatives are equal to zero can be easily understood by looking at the metric. The new form uses upper indices on the far right-hand side. Lowering and dropping indices is a basic practice when using Einstein's notation, so there is no need to show the procedure.

As shown, the Ricci tensor can be obtained using the Christoffel symbols

$$R_{\sigma\nu} = R_{\sigma\rho\nu}^{\rho} = \partial_\rho \Gamma_{\sigma\nu}^{\rho} - \partial_\nu \Gamma_{\sigma\rho}^{\rho} + \Gamma_{\rho\alpha}^{\rho} \Gamma_{\sigma\nu}^{\alpha} - \Gamma_{\nu\alpha}^{\rho} \Gamma_{\sigma\rho}^{\alpha}. \tag{1.4}$$

using only the derivatives of Γ, neglecting squared Christoffel symbols, knowing that $\eta^{\mu\alpha}\partial_\alpha\partial_\mu = \partial_t^2 - \partial_x^2 - \partial_y^2 - \partial_z^2 = \Box$, where the "box" operator is the d'Alembertian, and using contraction $h^\rho_\rho = \eta^{\rho\sigma}h_{\sigma\rho} = h$, the Ricci tensor of the linearised perturbed spacetime can be written in a more convenient form as

$$R_{\mu\nu} \simeq \partial_\rho\Gamma^\rho_{\mu\nu} - \partial_\nu\Gamma^\rho_{\mu\rho} = \frac{1}{2}\left(\partial_\rho\partial_\mu h^\rho{}_\nu + \partial_\rho\partial_\nu h^\rho{}_\mu - \partial_\mu\partial_\nu h - \Box h_{\mu\nu}\right). \tag{1.5}$$

The Einstein tensor $G_{\mu\nu}$ can be calculated directly from the Ricci tensor and the Ricci scalar, which is defined as

$$R = g^{\mu\nu}R_{\mu\nu} = \partial_\rho\partial_\sigma h^{\rho\sigma} - \Box h. \tag{1.6}$$

Using a known formula, $G_{\mu\nu}$ is calculated as follows:

$$G_{\mu\nu} = R_{\mu\nu} - \frac{1}{2}\eta_{\mu\nu}R \tag{1.7}$$

$$= \frac{1}{2}\left(\partial_\rho\partial_\mu h^\rho{}_\nu + \partial_\rho\partial_\nu h^\rho{}_\mu - \partial_\mu\partial_\nu h - \Box h_{\mu\nu} - \eta_{\mu\nu}\partial_\rho\partial_\mu h^{\mu\rho} + \eta_{\mu\nu}\Box h\right) \tag{1.8}$$

The final step is to insert the derived parts. The final equation of motion is as follows:

$$R_{\mu\nu} - \frac{1}{2}R\,g_{\mu\nu} + \Lambda g_{\mu\nu} = \frac{8\pi G}{c^4}T_{\mu\nu}, \tag{1.9}$$

$$\partial_\rho\partial_\mu h^\rho{}_\nu + \partial_\rho\partial_\nu h^\rho{}_\mu - \partial_\mu\partial_\nu h - \Box h_{\mu\nu} - \eta_{\mu\nu}\partial_\rho\partial_\mu h^{\mu\rho} + \eta_{\mu\nu}\Box h = \frac{16\pi G}{c^4}T_{\mu\nu}. \tag{1.10}$$

1.2 The Lorentz gauge condition

The process will begin with the introduction of a "trace-reversed" perturbation tensor (in 4-dimensional spacetime) $\phi_{\mu\nu}$. The raw form definition is as follows:

$$\phi_{\mu\nu} = h_{\mu\nu} - \frac{1}{2}\eta_{\mu\nu}h \tag{1.11}$$

Applying $\eta^{\mu\nu}$ to both sides, the (1.11) gives a useful relation

$$\phi = -h \quad \rightarrow \quad h_{\mu\nu} = \phi_{\mu\nu} - \frac{1}{2}\eta_{\mu\nu}\phi. \tag{1.12}$$

This finding suggests that the metric perturbation and the trace-reversed perturbation, $h_{\mu\nu}$ and $\phi_{\mu\nu}$, contain the same information. Substituting $\phi_{\mu\nu}$ into (1.10) results in the following transformation of the form:

$$\partial_\rho\partial_\mu\phi^\rho{}_\nu + \partial_\rho\partial_\nu\phi^\rho{}_\mu - \Box\phi_{\mu\nu} - \eta_{\mu\nu}\partial_\rho\partial_\mu\phi^{\mu\rho} = \frac{16\pi G}{c^4}T_{\mu\nu}. \tag{1.13}$$

The left-hand side is reduced to four terms [1]. A more advantageous configuration of the equation is achieved when the index ρ is lowered. The form is hereby:

$$\partial_\rho\partial_\nu\phi^\rho{}_\mu - \Box\phi_{\mu\nu} = \frac{16\pi G}{c^4}T_{\mu\nu}. \tag{1.14}$$

Now it is time to choose a gauge. Gauge fixing is a mathematical procedure that is used to reduce excess degrees of freedom, and it is a fundamental concept in numerous areas of physics, including quantum mechanics and electromagnetism. In essence, this approach is based on the premise that a field variable can be expressed as a function of another variable, along with a minor additional term that symbolises coordinate or gauge freedom. In the present case, two coordinate systems are introduced, denoted by x_μ and x'_μ. The coordinates differ by a small displacement $\xi^\mu(x^\nu)$. This deviation is characterised as four functions of the same order as the metric fluctuations, denoted by $h_{\mu\nu}$ within a four-dimensional spacetime. The equations are:

$$x^{\mu\prime} = x^\mu + \xi^\mu(x^\nu)\,. \tag{1.15}$$

The following definition of a derivative is provided, with the proviso that lower-order derivatives and higher-order terms are to be neglected[2]:

$$\frac{\partial x^\mu}{\partial x^{\nu\prime}} = \delta^\mu_\nu - \partial_\nu\xi^\mu, \quad \frac{\partial x^{\mu\prime}}{\partial x^\nu} = \delta^\mu_\nu + \partial_\nu\xi^\mu. \tag{1.16}$$

1. Detailed explanation in Appendix A.1.1
2. Detailed explanation in Appendix A.1.2

The derivation of the coordinate system is dependent on the Kronecker delta, given that it is equal to one when differentiated by itself and equal to zero when differentiated by other coordinates. In accordance with the established theme, the derivative of ξ^μ is in covariant formalism Continuing with the change of coordinates, the metric transforms as

$$g'_{\mu\nu}(x') = \frac{\partial x^\rho}{\partial x^{\mu'}} \frac{\partial x^\sigma}{\partial x^{\nu'}} g_{\rho\sigma}(x) = \left(\delta^\rho_\mu - \partial_\mu \xi^\rho\right)\left(\delta^\sigma_\nu - \partial_\nu \xi^\sigma\right)\left(\eta_{\rho\sigma} + h_{\rho\sigma}\right) \simeq \eta_{\mu\nu} + h_{\mu\nu} - \partial_\mu \xi_\nu - \partial_\nu \xi_\mu = \eta_{\mu\nu} + h'_{\mu\nu}\,, \tag{1.17}$$

where $h'_{\mu\nu} = h_{\mu\nu} - \partial_\mu \xi_\nu - \partial_\nu \xi_\mu$. This is just for a clear arrangement and similarity to the starting metric with a small perturbation. The definition of a metric (coordinate invariance) naturally points to the gauge condition in trace-reversed perturbation[3],

$$\phi'_{\mu\nu} = \phi_{\mu\nu} - \partial_\mu \xi_\nu - \partial_\nu \xi_\mu + \eta_{\mu\nu} \partial_\lambda \xi^\lambda. \tag{1.18}$$

In the field of general relativity, the conventional approach to gauge fixing involves the adoption of a *harmonic gauge condition*. The name is derived from the coordinate functions x_μ and x'_μ satisfying the d'Alembert equation, which is just Laplace's equation in spacetime. This equation is a component of a wave equation, the solution to which is a harmonic wave. Mathematical notation is employed to express the following:

$$\Box x^\mu = 0. \tag{1.19}$$

The condition can now be explicitly expanded using the definition of the d'Alembertian operator, which is given by the formula $\Box = \nabla^\alpha \nabla_\alpha$. The covariant derivative takes the form $\nabla_\alpha x^\mu = \partial_\alpha x^\mu + \Gamma^\mu_{\alpha\nu} x^\nu$ for a four-vector and $\nabla_\alpha \omega_\mu = \partial_\alpha \omega_\mu - \Gamma^\nu_{\alpha\mu} \omega_\nu$ for a one-form. The concept of a four-vector is relatively uncomplicated, given that the term *four* is derived from three spatial and one time dimension. The one-form is not as trivial. In essence, it is defined as a function of a single vector that yields a scalar (real number) as a result.

3. Detailed explanation in Appendix A.1.3

It is also noteworthy that the covariant derivative of a scalar is equivalent to a partial derivative. This is why the definition of covariant differentiation for a four-vector and a one-form includes a partial differentiation on the right-hand side. This is because the x^μ is just a scalar function, not a component of a vector. The condition, therefore, expands with the now gained knowledge about covariant derivatives as

$$0 = \Box x^\mu = \eta^{\rho\sigma}(\partial_\rho \partial_\sigma x^\mu - \Gamma^\lambda_{\rho\sigma}\partial_\lambda x^\mu) = -\eta^{\rho\sigma}\Gamma^\lambda_{\rho\sigma}. \tag{1.20}$$

The expanded condition in a weak field is easily obtained by inserting (1.3) into the equation above, thus:

$$0 = \frac{1}{2}\eta^{\rho\sigma}\eta^{\lambda\alpha}(\partial_\rho h_{\sigma\alpha} + \partial_\sigma h_{\rho\alpha} - \partial_\alpha h_{\rho\sigma}) = \partial_\rho h^\rho_\alpha - \frac{1}{2}\partial_\alpha h. \tag{1.21}$$

The condition is then applied to the linearised equation of motion (1.10). The left-hand side transforms to $\frac{1}{2}\partial_\nu\partial_\mu h = \frac{1}{2}\eta_{\mu\nu}\Box h$ and the fifth term transforms to $-\partial_\rho\partial_\mu h^\rho_\nu = -\frac{1}{2}\eta_{\mu\nu}\Box h$.

Imposing the Lorentz gauge onto the linearised equation of motion (1.10) gives the form of

$$\Box h_{\mu\nu} - \frac{1}{2}\eta_{\mu\nu}\Box h = -\frac{16\pi G}{c^4}T_{\mu\nu}, \tag{1.22}$$

or using (1.11) for an even more compact form

$$\Box \phi_{\mu\nu} = -\frac{16\pi G}{c^4}T_{\mu\nu}. \tag{1.23}$$

Applying the vacuum solution of the EFE ($R_{\mu\nu} = 0$), the gauge defined by x'_μ and the Lorenz gauge gives the following conditions:

$$\Box h_{\mu\nu} = 0, \qquad \Box \phi_{\mu\nu} = 0, \qquad \Box \xi^\mu = 0. \tag{1.24}$$

Moreover, raising the indices and inserting the trace-reversed tensor into (1.21) results in an alternative formulation of the Lorentz gauge condition:

$$\partial_\rho \phi^{\rho\nu} = 0. \tag{1.25}$$

1.3 The metric

Firstly, the application of linearised gravity to the gravitational field of an isolated mass in the Newtonian limit will be considered. It is assumed that the energy-momentum tensor (henceforth referred to as the T-M tensor) is dominated by the energy density, i.e. $\varepsilon = \rho c^2$ as seen in the non-relativistic form of the tensor

$$T_{\mu\nu} = \begin{pmatrix} \varepsilon & 0 & 0 & 0 \\ 0 & 0 & 0 & 0 \\ 0 & 0 & 0 & 0 \\ 0 & 0 & 0 & 0 \end{pmatrix}. \tag{1.26}$$

The matter remains practically static or moves at a sufficiently gradual rate for the time derivatives to be negligible. In accordance with the chosen convention, this results in the equation $\Box = -\nabla^2$ in the chosen convention $+---$. The spacetime is therefore said to be "asymptotically flat", in the sense that it acts as flat Minkowski spacetime over large distances. This assumption serves to modify the compact form of a linearised equation of motion with the Lorentz gauge, as expressed in equation (1.23), to

$$\nabla^2 \phi_{00} = \frac{16\pi G}{c^2}\rho. \tag{1.27}$$

The implementation of the gravitational Poisson equation, which can be expressed as $\nabla^2\Phi = 4\pi G\rho$ [4] where Φ is the gravitational potential, gives

$$\phi_{00} = \frac{4\Phi}{c^2}. \tag{1.28}$$

The left-hand side is labelled ϕ_{00} due to the negligible nature of the other components, a determination that is supported by the NR form of the T-M tensor. It is also evident that $\phi_{00} = \phi$ and $h_{i0} = \phi_{i0} - \frac{1}{2}\eta_{i0}\phi = 0$. In this context, the indexes $i = 1, 2, 3$ represent the spatial components of the metric. This immediately gives

$$h_{\mu\nu} = \frac{2\Phi}{c^2}\delta_{\mu\nu}. \tag{1.29}$$

4. Unfortunately, the letter "phi" had already been employed for the trace-reversed perturbation, as ϕ. To clarify the distinction between the two, capitalisation was used.

Directly following the initial definition of the metric with small perturbation $g_{\mu\nu} \simeq \eta_{\mu\nu} + h_{\mu\nu}$, where the Minkowski spacetime metric is $c^2\mathrm{d}t^2 - \mathrm{d}x^2 - \mathrm{d}y^2 - \mathrm{d}z^2$ (once again, for the chosen convention), we have the metric form

$$\mathrm{d}s^2 = \left(c^2 + 2\Phi\right)\mathrm{d}t^2 - \left(1 + \frac{2\Phi}{c^2}\right)\left(\mathrm{d}x^2 + \mathrm{d}y^2 + \mathrm{d}z^2\right) \tag{1.30}$$

of a perturbed spacetime in this weak-field limit.

1.4 Application of the weak-field limit to gravitational radiation

The description of the formalism of the weak-field limit applied to GR operates on the assumption that the perturbation within a vacuum solution ($\Box\phi_{\mu\nu} = 0$) radiates plane waves in the following form:

$$\phi_{\mu\nu} = A_{\mu\nu}\,\mathrm{e}^{\mathrm{i}k_\alpha x^\alpha} = A_{\mu\nu}\,\mathrm{e}^{-\mathrm{i}(k_i x^i - \omega t)}\,. \tag{1.31}$$

The $A_{\mu\nu}$ is a constant and symmetric spacetime tensor of second order, consisting of ten independent components known as the *polarisation tensor*. It includes information about the amplitude and polarisation properties of GWs. The k_α is the wave-vector, defined as $k_0 = k^0 = \omega/c$, $k_i = -k^i$. Subsequently, the flat-space d'Alembertian applied to a scalar complex 4-exponential results in

$$\Box\phi_{\mu\nu} = \eta^{\alpha\beta}\partial_\alpha\partial_\beta\phi_{\mu\nu} = \eta^{\alpha\beta}\partial_\alpha(\mathrm{i}k_\beta\phi_{\mu\nu}) = -\eta^{\alpha\beta}k_\alpha k_\beta\phi_{\mu\nu} = -k_\alpha k^\alpha\phi_{\mu\nu}. \tag{1.32}$$

The final expression is equal to zero due to the vacuum solution, as assumed at the commencement of this subsection. This means that

$$0 = -k_\alpha k^\alpha\phi_{\mu\nu}. \tag{1.33}$$

A null component is present. The $\phi_{\rho\nu}$ cannot be set to zero, as this would result in nothing to study/analyse. Consequently, the only solution to this equation is

$$k_\alpha k^\alpha = 0. \tag{1.34}$$

The propagation speed of gravitational waves (henceforth referred to as GWs) is equivalent to the speed of light (by using $k_0 = k^0 = \omega/c$ and inserting it into the equation (1.34)). Furthermore, redefining k_0 in terms of c and k results in a form that is strikingly similar to the phase velocity on the right-hand side. In a similar fashion, the group velocity is obtained. In this process, the angular frequency, denoted by the symbol ω, is placed on the right-hand side and differentiated by the wave-vector k. The final forms are

$$v_{\mathrm{p}} = \frac{\omega}{k} = c, \qquad v_{\mathrm{g}} = \frac{\partial \omega}{\partial k} = c\,. \tag{1.35}$$

It can thus be deduced that the group and phase velocities are equivalent to the speed of light. This straightforward derivation of the characteristics of the plane wave does not encompass all of the possibilities for general solutions. It can be posited that a substantial quantity of plane waves can be employed to solve the linear wave equations derived earlier (1.24). The utilisation of the alternative Lorentz gauge condition ($\partial_\rho \phi^{\rho\nu} = 0$) on the form of the assumed plane waves results in the following equation:

$$0 = \partial_\mu (A^{\mu\nu}\, \mathrm{e}^{\mathrm{i}k_\alpha x^\alpha}) = \mathrm{i}k_\mu A^{\mu\nu}\, \mathrm{e}^{\mathrm{i}k_\alpha x^\alpha}. \tag{1.36}$$

which is only satisfied if

$$k_\mu A^{\mu\nu} = 0. \tag{1.37}$$

Consequently, the wave vector k_μ can be regarded as orthogonal to the polarisation tensor $A^{\mu\nu}$, thereby reducing the number of independent components from ten to six. Utilising the final equation solely from the triad in equation (1.24) yields the plane wave solution for the displacement

$$\xi_\mu = B_\mu\, \mathrm{e}^{\mathrm{i}k_\sigma x^\sigma}. \tag{1.38}$$

where the B_μ are constant coefficients and the k_α is the wave four-vector. Using the gauge condition in trace reversed perturbation (1.18), an equation for a polarisation tensor $A'_{\mu\nu}$ is formed

$$A'_{\mu\nu} = A_{\mu\nu} - \mathrm{i}k_\mu B_\nu - \mathrm{i}k_\nu B_\mu + \mathrm{i}\eta_{\mu\nu} k_\lambda B^\lambda. \tag{1.39}$$

Raising the indices by $\eta^{\mu\nu}$ results in a more manageable and clearer equation

$$A'^{\mu}{}_{\mu} = A^{\mu}{}_{\mu} + 2\mathrm{i}k_{\lambda}B^{\lambda}. \tag{1.40}$$

The representation of B^{λ} in the form containing the Minkowski metric ($B_{\sigma}\eta^{\sigma\lambda}$) can reveal which terms are relevant. The Minkowski metric has non-zero values only on the diagonal. It is evident that the terms where $\sigma = \lambda$ are the only applicable ones. The $A'_{\mu\nu}$ is commonly referred to as the amplitude of GWs. The construction of the matrix transformation is now possible:

$$\begin{pmatrix} \frac{1}{2}A'^{\mu}{}_{\mu} \\ A'_{01} \\ A'_{02} \\ A'_{03} \end{pmatrix} = \begin{pmatrix} \frac{1}{2}A^{\mu}{}_{\mu} \\ A_{01} \\ A_{02} \\ A_{03} \end{pmatrix} + \mathrm{i} \begin{pmatrix} \frac{\omega}{c} & -k_1 & -k_2 & -k_3 \\ -k_1 & -\frac{\omega}{c} & 0 & 0 \\ -k_2 & 0 & -\frac{\omega}{c} & 0 \\ -k_3 & 0 & 0 & -\frac{\omega}{c} \end{pmatrix} \begin{pmatrix} B_0 \\ B_1 \\ B_2 \\ B_3 \end{pmatrix}, \tag{1.41}$$

The next step is to adjust the coordinate system so that these two conditions are met.

$$A'^{\mu}{}_{\mu} = 0, \qquad A'_{0\nu} = 0. \tag{1.42}$$

The Lorentz gauge can therefore be imposed on the plane wave form in equation (1.36) by taking the following steps,

$$\begin{aligned} k^{\mu}A'_{\mu\nu} &= k^{\mu}A_{\mu\nu} - \mathrm{i}k^{\mu}k_{\mu}B_{\nu} - \mathrm{i}k^{\mu}k_{\nu}B_{\mu} + \mathrm{i}\eta_{\mu\nu}k^{\mu}k_{\lambda}B^{\lambda} = \\ &= 0 - 0 - \mathrm{i}k_{\nu}\left(k^{\mu}B_{\mu} - k_{\lambda}B^{\lambda}\right) = 0 \quad \rightarrow \quad k^{\mu}A'_{\mu\nu} = 0. \end{aligned} \tag{1.43}$$

2 Polarisation of gravitational waves

At this moment, the Lorentz gauge was instrumental in reducing the ten independent components to six, a number that proved to be particularly convenient. However, for calculations, a larger reduction would be ideal, so the transverse-traceless gauge (hereafter referred to as a T-T gauge) is introduced. The initial step in this process is to select a simple set of coordinates. This ensures that the plane of GWs is propagating in the third special axis, i.e. $x^\mu = x^3$. The selection of the null wave-vector solution will result in the following outcome:

$$k^\mu = \left(\frac{\omega}{c}, 0, 0, x^3\right) = \left(\frac{\omega}{c}, 0, 0, \frac{\omega}{c}\right). \tag{2.1}$$

The condition given by equation (1.43) now yields the result $k^0 A'_{0\nu} + k^3 A'_{3\nu} = 0$. Combined with the second equation in (1.42) , this creates a new condition:

$$A'_{3\nu} = 0. \tag{2.2}$$

This process continues to reduce the independent terms in the $A'_{\mu\nu}$ to four, specifically to A'_{11}, A'_{12}, A'_{21}, and A'_{22}. In addition, it can be demonstrated that due to the symmetry of the tensor, the following equation is true: $A'_{12} = A'_{21}$. Finally, the first equation in (1.42) demonstrates that the tensor is traceless. The final condition can be derived through a straightforward calculation,

$$A'^{\mu}_{\ \mu} = \eta^{\mu\nu} A'_{\mu\nu} = A'_{00} - A'_{11} - A'_{22} - A'_{33} = 0 \quad \rightarrow \quad A'_{22} = -A'_{11}. \tag{2.3}$$

The tensor $A'_{\mu\nu}$ can now be written as

$$A'_{\mu\nu} = \begin{pmatrix} 0 & 0 & 0 & 0 \\ 0 & A'_{11} & A'_{12} & 0 \\ 0 & A'_{12} & -A'_{11} & 0 \\ 0 & 0 & 0 & 0 \end{pmatrix}. \tag{2.4}$$

In this configuration, the plane is entirely characterised by angular frequency ω and the two components A'_{11} and A'_{12}. This T-T gauge

is also referred to as the radiation gauge. In this particular gauge, the trace-reversed perturbation $\phi_{\mu\nu}$ is valid because the $A'_{\mu\nu}$ is. Subsequently, it can be demonstrated that the quantity in question is equivalent to the trace-reversed $h_{\mu\nu}$.

$$\phi^{TT}_{\mu\nu} = h^{TT}_{\mu\nu}. \tag{2.5}$$

Thanks to this, the two terms can be used interchangeably. To simplify and clarify the subject, the $A_+ = A'_{11}$ and $A_\times = A'_{12}$. This means

$$\boldsymbol{A} = \begin{pmatrix} 0 & 0 & 0 & 0 \\ 0 & A_+ & A_\times & 0 \\ 0 & A_\times & -A_+ & 0 \\ 0 & 0 & 0 & 0 \end{pmatrix}, \qquad h_{\mu\nu} = \boldsymbol{A}\, \mathrm{e}^{ik_\sigma x^\sigma}. \tag{2.6}$$

It is therefore possible to utilise these to calculate the amplitudes of arbitrary GWs. The metric associated with the GWs within the gauge is

$$\begin{aligned} \mathrm{d}s^2 &= g_{\mu\nu}\, \mathrm{d}x^\mu \mathrm{d}x^\nu = \\ &= c^2\, \mathrm{d}t^2 - \left(1 + A_+ \mathrm{e}^{ik_\sigma x^\sigma}\right) (\mathrm{d}x^1)^2 - 2A_\times \mathrm{e}^{ik_\sigma x^\sigma} \mathrm{d}x^1 \mathrm{d}x^2 - \\ &- \left(1 - A_+ \mathrm{e}^{ik_\sigma x^\sigma}\right) (\mathrm{d}x^2)^2 - (\mathrm{d}x^3)^2. \end{aligned} \tag{2.7}$$

To provide a more effective illustration, an example involving test particles at the space coordinates (x^1, x^2, x^3) will be used. The test particles will move according to the passing of a linearly polarised wave with polarisation $+$. In the direction of x^1, the particles oscillate in said direction; in the direction of x^2, the particles oscillate in the counter-phase. Finally, in the third direction, x^3, the particles remain unaffected as the wave propagates in this direction.

It can thus be demonstrated that the distance element for the first and second directions differs from each other solely by a sign; for example,

$$\mathrm{d}x^1 \approx \left(1 + \frac{1}{2} A_+ \mathrm{e}^{ik_\sigma x^\sigma}\right) \mathrm{d}x^1_0 \qquad \mathrm{d}x^2 \approx \left(1 - \frac{1}{2} A_+ \mathrm{e}^{ik_\sigma x^\sigma}\right) \mathrm{d}x^2_0. \tag{2.8}$$

The $\times$ polarised wave oscillates along the axes that have been rotated by 45 degrees, while the third direction remains unaltered. The choice

of sign for the tensor components, namely $\times$ and $+$, may be regarded as a subtle indication of the direction of oscillation of the particles. This is a concept that is both intuitive and of practical use in the broader context. Moreover, it is noteworthy that polarisation remains constant under a 180° rotation, a property that lends itself to certain advantageous applications.

3 Gravitational waves emitted from a two-body system

This chapter contains the derivation of the energy and momentum of GWs in a two-body system.

3.1 Energy of the gravitational waves

To derive the energy, certain assumptions must be made. Specifically, the vacuum EFEs are considered to second order, as well as the metric with small perturbations. The aim is to determine how the result can be interpreted as an E-M tensor. Einstein's tensor (henceforth referred to as ET) expanded to the first order of $h_{\mu\nu}$ is $G^{(1)}_{\mu\nu}[\eta + h] = 0$ (because the ET contains the Ricci tensor and scalar, and, as previously mentioned, the vacuum solution is $R_{\mu\nu} = 0$). It is evident that, given the utilisation of second-order EFEs, the metric is unable to neglect the second-order perturbations. Consequently, the revised metric is expressed as follows:

$$g_{\mu\nu} = \eta_{\mu\nu} + h_{\mu\nu} + h^{(2)}_{\mu\nu}. \tag{3.1}$$

The quantity $h^{(2)}_{\mu\nu}$ is referred to as the second-order perturbation. The EFEs are comprised of all terms that incorporate the quadratic form $h_{\mu\nu}$ and the linear $h^{(2)}_{\mu\nu}$. The elimination of all cross-terms (due to their potential to exceed the second order) results in the following equation:

$$G^{(1)}_{\mu\nu}[\eta + h^{(2)}] + G^{(2)}_{\mu\nu}[\eta + h] = 0. \tag{3.2}$$

The $G^{(2)}_{\mu\nu}$ is a component of the ET, which is of second order in the metric perturbation. The second-order Ricci tensor has been demonstrated to be a reliable computational tool in this regard, given its incorporation of non-linear components. The used equation is

$$R^{(2)}_{\mu\nu} = \partial_\rho \Gamma^\rho_{\mu\nu} - \partial_\nu \Gamma^\rho_{\mu\rho} + \Gamma^\rho_{\rho\lambda}\Gamma^\lambda_{\mu\nu} - \Gamma^\rho_{\mu\lambda}\Gamma^\lambda_{\nu\rho}\,, \tag{3.3}$$

from the linear tensor method employed to derive the vacuum solution in Chapter 1. Firstly, the calculation of the final two non-linear terms is

$$\begin{aligned}\Gamma^{\rho}_{\rho\lambda}\Gamma^{\lambda}_{\mu\nu} &= \Gamma^{\lambda}_{\mu\nu}\left[\tfrac{1}{2}\eta^{\rho\sigma}\left(\partial_\rho h_{\lambda\sigma}+\partial_\lambda h_{\rho\sigma}-\partial_\sigma h_{\rho\lambda}\right)\right]\\ &= \Gamma^{\lambda}_{\mu\nu}\tfrac{1}{2}\left(\partial_\rho h^{\rho}_{\lambda}+\partial_\lambda h^{\rho}_{\rho}-\partial_\sigma h^{\sigma}_{\lambda}\right)=0, \qquad (3.4)\\ -\Gamma^{\rho}_{\mu\lambda}\Gamma^{\lambda}_{\nu\rho} &= \frac{1}{4}(\partial_\mu h^{\rho\sigma})(\partial_\nu h_{\rho\sigma})+\frac{1}{2}\partial^\sigma(h^{\rho}_{\mu}\partial_\rho h_{\nu\sigma})\\ &\quad -\frac{1}{2}\partial^\sigma(h^{\rho}_{\mu}\partial_\sigma h_{\nu\rho})+\frac{1}{2}h^{\rho}_{\mu}\partial^\sigma\partial_\sigma h_{\nu\rho}\,. \qquad (3.5)\end{aligned}$$

In equation (3.4), the first and third terms are shown to cancel each other through the application of symmetry in the metric, $\eta^{\alpha\beta}=\eta^{\beta\alpha}$. Therefore, the identity used is $\eta^{\rho\sigma}\partial_\rho h_{\lambda\sigma}=\eta^{\sigma\rho}\partial_\sigma h_{\lambda\rho}$, and the second term is rendered zero by virtue of the traceless selection of the gauge. The equation (3.5) has its calculation and further explanation in Appendix A.2.1. The linear components were previously examined in the first chapter (final form shown in (1.5)). The combination of these components results in the following equation:

$$\begin{aligned}R^{(2)}_{\mu\nu} = \tfrac{1}{2}\Big[&\partial_\rho\partial_\mu h^{\rho}{}_{\nu}+\partial_\rho\partial_\nu h^{\rho}{}_{\mu}-\partial_\mu\partial_\nu h-\Box h_{\mu\nu}-\\ &-\tfrac{1}{2}(\partial_\mu h^{\rho\sigma})(\partial_\nu h_{\rho\sigma})+\partial^\sigma\big(h^{\rho}_{\mu}\partial_\rho h_{\nu\sigma}\big)-\partial^\sigma\big(h^{\rho}_{\mu}\partial_\sigma h_{\nu\rho}\big)+h^{\rho}_{\mu}\Box h_{\nu\rho}\Big].\end{aligned} \qquad (3.6)$$

The D'Alembertian symbol remains synonymous with the equation $\Box=\partial^\sigma\partial_\sigma=\partial_\sigma\partial^\sigma$. The Ricci scalar is derived by contracting the Ricci tensor with the tensor $\eta^{\mu\nu}$. Fortunately, the linear part has already been derived and presented in equation (1.6). Consequently, the contraction is applied exclusively to the second row of equation (3.6). The complete Ricci scalar is

$$\begin{aligned}R^{(2)} = \partial_\rho\partial_\mu h^{\mu\rho}-\Box h-&\\ -\tfrac{1}{2}\Big[&\tfrac{1}{2}(\partial^\nu h^{\rho\sigma})(\partial_\nu h_{\rho\sigma})+\partial^\sigma(h^{\nu\rho}\partial_\rho h_{\nu\sigma})-\partial^\sigma(h^{\nu\rho}\partial_\sigma h_{\nu\rho})+h^{\nu\rho}\Box h_{\nu\rho}\Big].\end{aligned} \qquad (3.7)$$

Knowing that, $G^{(2)}_{\mu\nu} = R^{(2)}_{\mu\nu} - \frac{1}{2}\eta_{\mu\nu}R^{(2)}$ and $G^{(1)}_{\mu\nu}(\eta + h^{(2)}) = \frac{8\pi G}{c^4}t_{\mu\nu}$, while also following the equation (3.2), a simple definition arises:

$$G^{(2)}_{\mu\nu}(\eta + h) = -\frac{8\pi G}{c^4}t_{\mu\nu}. \tag{3.8}$$

The symbol $t_{\mu\nu}$ denotes the T-M tensor, a quantity that is specific to the gravitational field in the weak-field regime. It is imperative to note that this text does not aspire to derive any significant conservation condition; rather, it will present the result. The rationale behind this approach is that incorporating the condition could expand the scope of the topic, potentially resulting in confusion or off-topic calculations. The modified T-M conservation condition is

$$\partial_\mu t^{\mu\nu} = 0. \tag{3.9}$$

Another method of simplifying the ET is averaging over a microscopic region, that is to say $[\int_a^b f(x)\,\mathrm{d}x]/(b-a)$, where the limits of integration a and b values are very small. This premise is rooted in the initial hypothesis that the perturbation $h_{\mu\nu}$ is also very small. Furthermore, if the GW's wavelength is significantly larger than the selected region, $b - a$, then the functions $f(a)$ and $f(b)$ will be practically indistinguishable. As previously mentioned, it is possible to neglect certain terms on the right-hand side of the equation for the Ricci scalar, as expressed in Equations (3.6) and (3.7). Thanks to $\partial_\mu h^\mu_\alpha = 0$, $h = h^\alpha_\alpha = 0$, and $\Box h_{\mu\nu} = 0$, the initial four terms and the concluding term within the specified equation 3.6 are rendered null. Additionally, it can be observed that the third and second-to-last terms also become null due to the neglect of the average of the total derivative, as previously outlined. As is the case with equation (3.7), the initial term within the square brackets also disappears as a consequence of the identical microscopic condition that exists within the averaged value. It is imperative to recall that $u'v = (uv)' - uv'$ where the middle averaged term vanishes, so $u'v \simeq -uv'$. This means

$$-\frac{1}{4}\left\langle(\partial^\nu h^{\rho\sigma})(\partial_\nu h_{\rho\sigma})\right\rangle = \frac{1}{4}\left\langle h^{\rho\sigma}\Box h_{\rho\sigma}\right\rangle = 0. \tag{3.10}$$

After some refining, a single term is left, which is the fifth term on the right-hand side of the equation (3.6):

$$R^{(2)}_{\mu\nu}(\eta + h) = -\frac{1}{4}\left\langle (\partial_\mu h^{\rho\sigma})(\partial_\nu h_{\rho\sigma})\right\rangle = -\frac{8\pi G}{c^4} t_{\mu\nu}, \tag{3.11}$$

that is:

$$t_{\mu\nu} = \frac{c^4}{32\pi G}\left\langle (\partial_\mu h^{\rho\sigma})(\partial_\nu h_{\rho\sigma})\right\rangle. \tag{3.12}$$

The subsequent stage in this process is to ascertain the components of the T-M tensor, with the starting point being T_{00} to describe the energy density. It is possible to ascertain the total energy of gravitational radiation (henceforth referred to as GR) contained within the surface Σ of constant time by means of the zero-zero component. Utilising the symmetries inherent within the system, the origin of the GR is situated at the origin of the system. This is a particularly salient consideration when working with retarded time,

$$E = \int_\Sigma t_{00}\, \mathrm{d}^3\boldsymbol{x}. \tag{3.13}$$

Similarly, the energy loss per second, denoted by ΔE, can be calculated. Using sphere S with radius R through which the GR radiate and the fact that $T_{0\mu}$ components describe flux in the directions μ, the ΔE is defined as

$$\Delta E = \int_S t_{0\mu} n^\mu\, \mathrm{d}^2\boldsymbol{x}\, \mathrm{d}t. \tag{3.14}$$

In this instance, the integral can be considered as a double integral over a two-sphere at a distance r (similar to infinity) and an interval in time. Here, n^μ is a unit space-like vector normal to S. The transformation to spherical coordinates is then made, with $t_{0\mu}n^\mu$ becoming t_{0r}. The equation (3.14) is then rearranged as follows:

$$\frac{\mathrm{d}E}{\mathrm{d}t} = \int_S t_{0r} r^2\, \mathrm{d}\Omega. \tag{3.15}$$

The t_{0r}, according to (3.1) is

$$t_{0r} = \frac{c^4}{32\pi G}\left\langle (\partial_0 h^{\alpha\beta}_{TT})(\partial_r h^{TT}_{\alpha\beta})\right\rangle. \tag{3.16}$$

The amount of radiated energy ΔE can also be expressed in terms of radiated power P, such as

$$\Delta E = \int P \, \mathrm{d}t, \tag{3.17}$$

where the power P is given by the integrand of (3.15) in spherical coordinates.

Now, the application of the T-T gauge to the transverse perturbation changes it to the weak field perturbation, which is a significant assistance for subsequent utilisation in equation (3.1). The objective is to ascertain a T-T tensor q^{ij}_{TT} constructed from the quadrupole moment q^{ij}, determine the $T_{0\mu}$ component, and reverse q^{ij}_{TT} back to its initial form q^{ij} without any information. The initial step in this process is to project the quadrupole moment onto its traceless component Q^{ij}, where $\mathrm{Tr}\, Q_{ij} = Q^i_i = 0$,

$$Q^{ij} = q^{ij} - \frac{1}{3}\delta^{ij}\delta_{kl}q^{kl}, \tag{3.18}$$

which is just the subtraction of an appropriately scaled trace, removing all the trace components. To make traceless Q^{ij} also transversal, the projection operator

$$P^b_a(\boldsymbol{x}) = \delta^b_a - \frac{x^b x_a}{r^2}, \quad \text{which is equivalent to} \quad P^b_a(\boldsymbol{n}) = \delta^b_a - n^b n_a, \tag{3.19}$$

where $\boldsymbol{x} = \left(x^1, x^2, x^3\right)$, so $x^i x_i = r^2$, and $\boldsymbol{n} = \left(\frac{x^1}{r}, \frac{x^2}{r}, \frac{x^3}{r}\right)$, so $n^i n_i = 1$, that acts as

$$Q^{ij}_{TT} = P^i_a Q_{ab} P^j_b - \frac{1}{2} P_{ab} Q_{ab} P^{ij}, \tag{3.20}$$

is used[1].

The gravitational sources are very distant, so the approximation for the TT part of the metric perturbation $h^{TT}_{\alpha\beta}$ can be expressed as being

1. Detailed explanation and verification are in Appendix A.2.2

proportional to the second time derivative of the quadrupole moment $\ddot{Q}^{\alpha\beta}_{TT}$, such as $h^{TT}_{\alpha\beta} \sim \frac{2G}{c^4 r^2}\ddot{Q}^{TT}_{\alpha\beta}(t_{\text{ret}})$ (focusing on far-field behaviour) when assembling the equation (3.16). The derivatives of $h^{TT}_{\alpha\beta}$ needed are

$$\partial_0 h^{\alpha\beta}_{TT} = \frac{2G}{c^4 r}\frac{\partial}{\partial t}\left[\ddot{Q}^{\alpha\beta}_{TT}(t_{\text{ret}})\right] = \frac{2G}{c^4 r}\frac{\partial t_{\text{ret}}}{\partial t}\frac{\partial}{\partial t_{\text{ret}}}\left[\ddot{Q}^{\alpha\beta}_{TT}(t_{\text{ret}})\right], \tag{3.21}$$

$$\begin{aligned}\partial_r h^{TT}_{\alpha\beta} = \frac{2G}{c^4}\frac{\partial}{\partial r}\left[\frac{1}{r}\ddot{Q}^{\alpha\beta}_{TT}(t_{\text{ret}})\right] &= \frac{2G}{c^4 r}\frac{\partial t}{\partial r}\frac{\partial t_{\text{ret}}}{\partial t}\frac{\partial}{\partial t_{\text{ret}}}\left[\ddot{Q}^{\alpha\beta}_{TT}(t_{\text{ret}})\right] \\ &\quad - \frac{2G}{c^4 r^2}\left[\ddot{Q}^{TT}_{\alpha\beta}(t_{\text{ret}})\right].\end{aligned} \tag{3.22}$$

For a clearer arrangement, the definition of the derivative $\partial t_{\text{ret}}/\partial t$ in the form of $\frac{\partial t_{\text{ret}}}{\partial t} = \frac{c}{c-(\boldsymbol{n}\cdot\boldsymbol{u})_{\text{ret}}} = \left[\frac{1}{1-\dot{\boldsymbol{r}}\cdot\boldsymbol{n}}\right]_{\text{ret}}$ [2] is used, but since the source velocity β (the ratio v/c) is negligible in the far zone, it is assumed that $\partial t_{\text{ret}}/\partial t \approx 1$. Another chosen assumption comes from the spherical symmetry (one radial coordinate r). The radial derivative of the quadrupole ∂_r can be set equal to c times the time derivative ∂_t, except for the direct spatial derivative of r in the denominator:

$$\partial_0 h^{\alpha\beta}_{TT} = \frac{2G}{c^4 r}\left[\dddot{Q}^{\alpha\beta}_{TT}(t_{\text{ret}})\right], \tag{3.23}$$

$$\partial_r h^{TT}_{\alpha\beta} = \frac{2G}{c^5 r}\left[\dddot{Q}^{TT}_{\alpha\beta}(t_{\text{ret}})\right] - \frac{2G}{c^4 r^2}\left[\ddot{Q}^{TT}_{\alpha\beta}(t_{\text{ret}})\right]. \tag{3.24}$$

As previously stated, the source is located at a considerable distance; thus, the final term in equation (3.24) can be neglected due to the r^2 in the denominator.

The energy equation is revisited (alternatively termed the *total energy release* equation). Inserting the derived and calculated components into (3.15) gives

$$\begin{aligned}\frac{\mathrm{d}E}{\mathrm{d}t} &= \left\langle \int_S \frac{c^4}{32\pi G}\frac{4G^2}{c^9 r^2} r^2\, \dddot{Q}^{\alpha\beta}_{TT}\, \dddot{Q}^{TT}_{\alpha\beta}\, \mathrm{d}\Omega \right\rangle \\ &= \left\langle \int_S \frac{G}{8\pi c^5}\, \dddot{Q}^{\alpha\beta}_{TT}\, \dddot{Q}^{TT}_{\alpha\beta}\, \mathrm{d}\Omega \right\rangle.\end{aligned} \tag{3.25}$$

2. Detailed explanation in Appendix A.2.3

The objective is to attain a general solution to the integral. Firstly, the projection operator P with $P = P^2$ property is used [3],

$$\dddot{Q}_{ij}^{TT}\dddot{Q}_{TT}^{ij} = \left(P_i^a P_j^b - \frac{1}{2}P^{ab}P_{ij}\right)\left(P_c^i P_d^j - \frac{1}{2}P_{cd}P^{ij}\right)\ddot{Q}_{ab}\ddot{Q}^{cd}. \quad (3.26)$$

The two brackets with projection operators can be split into four terms, thanks to basic multiplication and work with Einstein notation. The last equation also uses $\frac{1}{2}P_i^i = 1$ similarly to Appendix (A.2.2). The resulting terms are

$$P_i^a P_j^b P_c^i P_d^j = P_c^a P_d^b, \qquad -\frac{1}{2}P_i^a P_j^b P_{cd}P^{ij} = -\frac{1}{2}P_{cd}P^{ab},$$
$$-\frac{1}{2}P^{ab}P_{ij}P_c^i P_d^j = -\frac{1}{2}P_{cd}P^{ab}, \qquad \frac{1}{4}P^{ab}P_{ij}P_{cd}P^{ij} = \frac{1}{2}P_{cd}P^{ab}. \quad (3.27)$$

In the equations, two pairs of projection operators recur. The calculation of both is

$$P_c^a P_d^b = \left(\delta_c^a - \frac{x^a x_c}{r^2}\right)\left(\delta_d^b - \frac{x^b x_d}{r^2}\right) =$$
$$= \delta_c^a\delta_d^b - \delta_c^a\frac{x^b x_d}{r^2} - \delta_d^b\frac{x^a x_c}{r^2} + \frac{x^a x^b x_c x_d}{r^4}, \quad (3.28)$$

$$P_{cd}P^{ab} = \left(\delta_{cd} - \frac{x_c x_d}{r^2}\right)\left(\delta^{ab} - \frac{x^a x^b}{r^2}\right) =$$
$$= \delta^{ab}\delta_{cd} - \delta^{ab}\frac{x_c x_d}{r^2} - \delta_{cd}\frac{x^a x^b}{r^2} + \frac{x^a x^b x_c x_d}{r^4}, \quad (3.29)$$

once again using Appendix A.2.2 as a guide. Putting these equations back into (3.26), while using only the first and second terms, as the

3. Detailed description is in Appendix A.2.2

third and fourth terms are subtracted in (3.27), gives

$$P_c^a P_d^b \,\dddot{Q}_{ab}\dddot{Q}^{cd} = \dddot{Q}_{ab}\dddot{Q}^{ab} - \frac{x^b x^d}{R^2}\,\dddot{Q}_{ab}\dddot{Q}^{a}{}_{d} - \frac{x^a x^c}{R^2}\,\dddot{Q}_{ab}\dddot{Q}_{c}{}^{b} + \frac{x^a x^b x^c x^d}{R^4}\,\dddot{Q}_{ab}\dddot{Q}_{cd}, \tag{3.30}$$

$$-\frac{1}{2}P_{cd}P^{ab}\,\dddot{Q}_{ab}\dddot{Q}^{cd} = -\frac{1}{2}\,\ddot{Q}\,\ddot{Q} + \frac{x_c x_d}{2R^2}\,\ddot{Q}\,\dddot{Q}^{cd} + \frac{x^a x^b}{2R^2}\,\dddot{Q}_{ab}\,\ddot{Q} - \frac{x^a x^b x^c x^d}{2R^4}\,\dddot{Q}_{ab}\dddot{Q}_{cd}. \tag{3.31}$$

The quadrupole moment of mass distribution is also traceless ($Q = 0$), so the equation (3.26) can be further modified as follows:

$$\dddot{Q}^{ij}_{TT}\dddot{Q}^{TT}_{ij} = \dddot{Q}_{ab}\dddot{Q}^{ab} - \frac{x^b x^d}{R^2}\dddot{Q}_{ab}\dddot{Q}^{a}_{d} - \frac{x^a x^c}{R^2}\dddot{Q}_{ab}\dddot{Q}^{b}_{c} + \frac{x^a x^c x^b x^d}{2R^4}\dddot{Q}_{ab}\dddot{Q}_{cd}. \tag{3.32}$$

The desired power $P = \mathrm{d}E/\mathrm{d}t$ is now only steps away, the next step being the integration of the found term over $\mathrm{d}\Omega$. The solution for a surface S with radius R is introduced to make the calculation easier [4]

$$\begin{aligned} \int \frac{\mathrm{d}\Omega}{4\pi}\, x^a x^b &= \frac{1}{3}R^2\,\eta^{ab}, \\ \int \frac{\mathrm{d}\Omega}{4\pi}\, x^a x^b x^c x^d &= \frac{1}{15}R^4\left(\eta^{ab}\eta^{cd} + \eta^{ac}\eta^{bd} + \eta^{ad}\eta^{bc}\right). \end{aligned} \tag{3.33}$$

4. Explanation in Appendix A.2.4

The calculation of the integral is then

$$\begin{aligned}\int \frac{\mathrm{d}\Omega}{4\pi}\,\dddot{Q}^{ij}_{TT}\dddot{Q}^{TT}_{ij} &= \dddot{Q}_{ab}\dddot{Q}^{ab} - \frac{1}{3}\eta^{bd}\,\dddot{Q}_{ab}\dddot{Q}^{a}{}_{d} - \frac{1}{3}\eta^{ac}\,\dddot{Q}_{ab}\dddot{Q}_{c}{}^{b} + \\ &\quad + \frac{1}{30}\left(\eta^{ab}\eta^{cd} + \eta^{ac}\eta^{bd} + \eta^{ad}\eta^{bc}\right)\dddot{Q}_{ab}\dddot{Q}_{cd} = \\ &= \dddot{Q}_{ab}\dddot{Q}^{ab} - \frac{2}{3}\,\dddot{Q}_{ab}\dddot{Q}^{ab} + \frac{1}{30}\left(\dddot{Q}\dddot{Q} + \dddot{Q}_{ab}\dddot{Q}^{ab}\right) + \\ &\quad + \frac{1}{30}\,\dddot{Q}_{ab}\dddot{Q}^{ba} = \\ &= \frac{2}{5}\,\dddot{Q}_{ab}\dddot{Q}^{ab}, \end{aligned} \tag{3.34}$$

where $Q = 0$ and $Q^{ab} = Q^{ba}$ once again apply. Inserting this result into the equation (3.25) gives a formula for quadrupole radiation first derived by Albert Einstein

$$\frac{\mathrm{d}E_{\mathrm{gw}}}{\mathrm{d}t} = \frac{G}{5c^5}\left\langle \dddot{Q}_{ab}\dddot{Q}^{ab}\right\rangle, \tag{3.35}$$

where the $\dddot{Q}_{ab}$ must be evaluated at the retarded time

3.2 Important parameters of emitted gravitational waves

This subsection is consistent with Section 3.2.1 of the preceding bachelor's thesis (Hergetová 2024) and includes detailed calculations and explanations to enhance the content. This was achieved with the assistance of the aforementioned sources, as referenced at the beginning of the theoretical introduction.

The primary step in this process is to establish the binary system that emits GWs. The binary system is characterised by a circular orbit in the xy plane. Each constituent element of the system possesses a distinct mass m_1 and/or m_2, and a separation a. This observation signifies that the components possess a reduced mass μ. The objects orbit each other with an angular frequency ω. The total orbital energy

E_{orb} of the binary system can also be defined. The definitions are as follows:

$$\begin{aligned} \mu &= \frac{m_1 m_2}{M}, \qquad \Omega = \sqrt{\frac{GM}{a^3}}, \\ E_{\text{orb}} &= \frac{1}{2}\left(m_1 a_1^2 + m_2 a_2^2\right)\Omega^2 - \frac{G m_1 m_2}{a} = -\frac{G\mu M}{2a}, \end{aligned} \tag{3.36}$$

where $M = m_1 + m_2$ is the total mass. In this analysis, a binary system with masses m_1 and m_2 is assumed to be isolated. It is also assumed that the relative coordinate x_0 is performing a circular orbit with a constant radius R in the xy plane. In the centre-of-mass frame, the x_0^i components are given as

$$x_0(t_{\text{ret}}) = R\cos\Omega t_{\text{ret}}, \qquad y_0(t_{\text{ret}}) = R\sin\Omega t_{\text{ret}}, \qquad z_0(t_{\text{ret}}) = 0. \tag{3.37}$$

The quadrupole mass moment components, defined as $q_{ij}(t) = \mu x_0^i(t) x_0^j(t)$, then take the form:

$$\begin{aligned} q_{11}(t_{\text{ret}}) = \mu R^2\cos^2\Omega t_{\text{ret}}, \qquad q_{22}(t_{\text{ret}}) = \mu R^2\sin^2\Omega t_{\text{ret}}, \\ q_{12}(t_{\text{ret}}) = \mu R^2\sin\Omega t_{\text{ret}}\cos\Omega t_{\text{ret}}, \end{aligned} \tag{3.38}$$

where, thanks to the symmetry, $q_{21}(t_{\text{ret}}) = q_{12}(t_{\text{ret}})$. Other components are equal to zero. By basic differentiation, the second and third time derivatives are obtained

$$\begin{aligned} \ddot{q}_{11}(t_{\text{ret}}) = -2\mu R^2\Omega^2\cos 2\Omega t_{\text{ret}}, \qquad \ddot{q}_{22}(t_{\text{ret}}) = 2\mu R^2\Omega^2\cos 2\Omega t_{\text{ret}}, \\ \ddot{q}_{12}(t_{\text{ret}}) = -2\mu R^2\Omega^2\sin 2\Omega t_{\text{ret}}, \end{aligned} \tag{3.39}$$

$$\begin{aligned} \dddot{q}_{11}(t_{\text{ret}}) = 4\mu R^2\Omega^3\sin 2\Omega t_{\text{ret}}, \qquad \dddot{q}_{22}(t_{\text{ret}}) = -4\mu R^2\Omega^3\sin 2\Omega t_{\text{ret}}, \\ \dddot{q}_{12}(t_{\text{ret}}) = -4\mu R^2\Omega^3\cos 2\Omega t_{\text{ret}}. \end{aligned} \tag{3.40}$$

The components are part of a 3×3 matrix. The third derivative matrix is traceless as the components on the diagonal subtract. According to (3.18), it is also equal to the $\dddot{Q}_{ij}$. Inserting it into the quadrupole

radiation formula (3.35), where the time derivative of the energy of GWs can be denoted as luminosity L_{gw}, gives

$$L_{\mathrm{gw}} = \frac{G}{5c^5}\left\langle \dddot{Q}_{ab}\dddot{Q}^{ab}\right\rangle = \frac{32G\mu^2R^4\Omega^6}{5c^5} = \frac{32G^4\mu^2M^3}{5c^5R^5}. \tag{3.41}$$

When the binary system loses energy by emitting radiation, the distance between the two bodies reduces at a rate

$$L_{\mathrm{gw}} = -\frac{\mathrm{d}E_{\mathrm{orb}}}{\mathrm{d}t} = -\frac{G\mu M}{2R^2}\frac{\mathrm{d}R}{\mathrm{d}t}, \quad \text{that is,} \quad \frac{\mathrm{d}R}{\mathrm{d}t} = -\frac{64G^3\mu M^2}{5c^5R^3}, \tag{3.42}$$

while the orbital frequency increases based on the decrease in the orbital distance as

$$\frac{\dot{f}}{f} = \frac{\dot{\Omega}}{\Omega} = -\frac{3\dot{R}}{2R}. \tag{3.43}$$

With the present separation of the two stars, which can be denoted R_{init}, and the equation (3.42), the GW inspiral time can be calculated as

$$t_{\mathrm{GW}} = -\frac{5c^5}{64G^3\mu M^2}\int_{R_{\mathrm{init}}}^{0} R^3\,\mathrm{d}R = \frac{5c^5R_{\mathrm{init}}^4}{256G^3\mu M^2} = \frac{5c^5M^{1/3}}{256G^{5/3}m_1m_2\Omega_{\mathrm{init}}^{8/3}}. \tag{3.44}$$

If $\dot{\Omega} \ll \Omega^2$, these calculations can be done in a quasi-circular motion regime; the orbit is very close to being circular, and orbital parameters such as radius are evolving more slowly than the orbital period. Modifying the equation (3.43) yields $\dot{R} = -\frac{2}{3}R\frac{\dot{\Omega}}{\Omega} = -\frac{2}{3}R\Omega\frac{\dot{\Omega}}{\Omega^2} = -\frac{2}{3}V_\phi\frac{\dot{\Omega}}{\Omega^2}$. If the quasi-circular approximation still holds, the $|\dot{R}|$ is much smaller than the tangential orbital velocity defined as $V_\phi = R\Omega$. To determine the amplitude of the GW, the operator P is applied to the traceless form

$$h_{ij}^{TT} = \frac{2G}{c^4r}\ddot{Q}_{ij}(t_{\mathrm{ret}}), \tag{3.45}$$

where in the TT gauge $h_{ij} = \phi_{ij}$ and $\ddot{Q}_{ij} = \ddot{q}_{ij}$. If the propagation of the GW is $\boldsymbol{z}$, then the P_{ij} operator becomes

$$P_{ij} = P_i^{\ j} = P^{ij} = \begin{pmatrix} 1 & 0 & 0 \\ 0 & 1 & 0 \\ 0 & 0 & 0 \end{pmatrix}_{ij},$$

$$\text{so} \qquad P_i^{\ a}\, \ddot{q}_{ab}\, P^j_{\ b} - \frac{1}{2} P_{ab}\, \ddot{q}_{ab}\, P^{ij} = \ddot{q}_{ij} - \frac{1}{2}\ddot{q}_{aa}\, P^{ij}$$

$$= \begin{pmatrix} \ddot{q}_{11} & \ddot{q}_{12} & 0 \\ \ddot{q}_{21} & \ddot{q}_{22} & 0 \\ 0 & 0 & 0 \end{pmatrix} - \frac{1}{2}\,\mathrm{Tr}(\ddot{q}) \begin{pmatrix} 1 & 0 & 0 \\ 0 & 1 & 0 \\ 0 & 0 & 0 \end{pmatrix}$$

$$= \begin{pmatrix} \dfrac{\ddot{q}_{11} - \ddot{q}_{22}}{2} & \ddot{q}_{12} & 0 \\ \ddot{q}_{21} & -\dfrac{\ddot{q}_{11} - \ddot{q}_{22}}{2} & 0 \\ 0 & 0 & 0 \end{pmatrix}, \tag{3.46}$$

because both n_x and n_y are zero, and $n^i n_j = 0$ if $i \neq j$, so $P^x_x = \delta^x_x = 1$, $P^y_y = \delta^y_y = 1$, and $P^z_z = \delta^z_z - n^z n_z = 1 - 1 = 0$. In the final P matrix, the two polarisation amplitudes of the GWs propagating in the direction z are evident. Their form, valued at the t_{ret}, is

$$h_+(t, \boldsymbol{z}) = \frac{G}{c^4 r}(\ddot{q}_{11} - \ddot{q}_{22}), \quad h_\times(t, \boldsymbol{z}) = \frac{2G}{c^4 r}\,\ddot{q}_{12}. \tag{3.47}$$

To calculate the amplitude of the GW within the standard Cartesian coordinate frame (x, y, z), when the wave is propagating in an arbitrary direction $\boldsymbol{n}$, it is necessary to introduce another orthogonal frame. The prime frame, denoted by the symbol (x', y', z'), is defined to be initially equivalent to the non-prime frame. The next step is to apply a series of two rotations. The first rotation is around the axis $z \equiv z'$. The second rotation is around the axis x'. Both frames are then inclined in both angular directions, that is, in both ϕ and θ. If the GW propagates in the prime frame along the axes z', then the propagation vector $\boldsymbol{n}$ has coordinates $n'_i = (0, 0, 1)$. In the non-prime frame, the vector takes the form $n_i = (\sin\theta\cos\phi, \sin\theta\sin\phi, \cos\theta)$. The complete geometric relationship between these two systems is defined by a rotation matrix,

denoted $\mathcal{R}$, which is the product of the individual rotation operators. The resulting rotation matrix $\mathcal{R}$ is constructed as follows:

$$\mathcal{R} = \begin{pmatrix} \cos\phi & \sin\phi & 0 \\ -\sin\phi & \cos\phi & 0 \\ 0 & 0 & 1 \end{pmatrix} \begin{pmatrix} 1 & 0 & 0 \\ 0 & \cos\theta & \sin\theta \\ 0 & -\sin\theta & \cos\theta \end{pmatrix} =$$

$$= \begin{pmatrix} \cos\phi & \cos\theta\sin\phi & \sin\theta\sin\phi \\ -\sin\phi & \cos\theta\cos\phi & \sin\theta\cos\phi \\ 0 & -\sin\theta & \cos\theta \end{pmatrix}. \tag{3.48}$$

When this prerequisite is applied to equation (3.47), it differs in the prime frame by the argument $(t, \boldsymbol{n})$. It replaces the $(t, \boldsymbol{z})$. The $\ddot{q}$'s are now also primed. The transformation of $\ddot{q}$ to its primed form is defined as $\ddot{q}'_{ij} = (\mathcal{R}^T \ddot{q}\, \mathcal{R})_{ij}$, where $\mathcal{R}^T$ is the transposed rotation matrix. The transformation of all non-zero components is then

$$\begin{aligned}
\ddot{q}'_{11} &= \ddot{q}_{11}\cos^2\phi - \ddot{q}_{12}\sin 2\phi + \ddot{q}_{22}\sin^2\phi, \\
\ddot{q}'_{12} &= \frac{\cos\theta\sin 2\phi}{2}\,\ddot{q}_{11} + \cos\theta\cos 2\phi\,\ddot{q}_{12} - \sin\theta\cos\phi\,\ddot{q}_{13} - \\
&\quad - \frac{\cos\theta\sin 2\phi}{2}\,\ddot{q}_{22} + \sin\theta\sin\phi\,\ddot{q}_{23}, \\
\ddot{q}'_{22} &= \cos^2\theta\sin^2\phi\,\ddot{q}_{11} + \cos^2\theta\sin 2\phi\,\ddot{q}_{12} - \sin 2\theta\sin\phi\,\ddot{q}_{13} + \\
&\quad + \cos^2\theta\cos^2\phi\,\ddot{q}_{22} - \sin 2\theta\cos\phi\,\ddot{q}_{23} + \sin^2\theta\,\ddot{q}_{33}.
\end{aligned} \tag{3.49}$$

Using all of this information, the two polarisation amplitudes of GWs in the primed frame are

$$\begin{aligned}
h_+(t, \boldsymbol{n}) = \frac{G}{c^4 r}\Big|&\ddot{q}_{11}\left(\cos^2\phi - \cos^2\theta\sin^2\phi\right) - \ddot{q}_{12}\sin 2\phi\left(1 + \cos^2\theta\right) + \\
&+ \ddot{q}_{13}\sin 2\theta\sin\phi + \ddot{q}_{22}\left(\sin^2\phi - \cos^2\theta\cos^2\phi\right) + \\
&+ \ddot{q}_{23}\sin 2\theta\cos\phi - \ddot{q}_{33}\sin^2\theta\Big|,
\end{aligned}$$

$$\begin{aligned}
h_\times(t, \boldsymbol{n}) = \frac{G}{c^4 r}\Big|&\left(\ddot{q}_{11} - \ddot{q}_{22}\right)\cos\theta\sin 2\phi + 2\,\ddot{q}_{12}\cos\theta\cos 2\phi - \\
&- 2\,\ddot{q}_{13}\sin\theta\cos\phi + 2\,\ddot{q}_{23}\sin\theta\sin\phi\Big|.
\end{aligned} \tag{3.50}$$

The angular distribution of the quadrupole radiation can be calculated using the following equations once q_{ij} is known.

As the evolution of the system is considered on a circular orbit in the xy plane, the modified metric defined as $g^{\mu\nu} \simeq \eta^{\mu\nu} - h^{\mu\nu}$ and already defined q_{ij} in (3.39) can be inserted into the calculated amplitudes seen in (3.50). Following the basic simplification of the algebraic expressions, the amplitudes take the following form:

$$h_+(t, \boldsymbol{n}) = \frac{4G\mu R^2\Omega^2}{c^4 r}\left(\frac{1+\cos^2\theta}{2}\right)\cos\left(2\Omega t_{\text{ret}} + 2\phi\right), \tag{3.51}$$

$$h_\times(t, \boldsymbol{n}) = \frac{4G\mu R^2\Omega^2}{c^4 r}\cos\theta\sin\left(2\Omega t_{\text{ret}} + 2\phi\right). \tag{3.52}$$

Another simplification comes from the idea that in this circular orbit approximation, where $\Omega\Delta t_{\text{ret}} = \Delta\phi$. The origin of time can be shifted, such as $\Omega t_{\text{ret}} + \phi \to \Omega t_{\text{ret}}$. Furthermore, the substitution of frequency f of GW (that is, twice the orbital frequency) is advantageous. The final form is as follows:

$$h_+(t, \boldsymbol{n}) = \frac{4G\mu R^2(\pi f)^2}{c^4 r}\left(\frac{1+\cos^2\theta}{2}\right)\cos\left(2\pi f t_{\text{ret}}\right), \tag{3.53}$$

$$h_\times(t, \boldsymbol{n}) = \frac{4G\mu R^2(\pi f)^2}{c^4 r}\cos\theta\sin\left(2\pi f t_{\text{ret}}\right). \tag{3.54}$$

It is now evident that if this source of GWs is observed from pole-on ($\theta = 0$, $\cos\theta = 1$), the amplitudes are identical, with a shifted phase of $\pi/2$ and circularly polarised. On the contrary, if the source is observed equator-on ($\theta = \pi/2$, $\cos\theta = 0$), the cross amplitude $h_\times$ is zero and vanishes, while the plus amplitude h_+ is of half the magnitude compared to the pole-on observation and is linearly polarised.

Following the angular acceleration and substituting (3.42), the relation for $\dot{\Omega}$ is

$$\dot{\Omega} = -\frac{3\Omega}{2R}\dot{R} = \frac{96G^{7/2}\mu M^{5/2}}{5c^5 R^{11/2}} = \frac{96G^{5/3}\left(\mu M^{2/3}\right)\Omega^{11/3}}{5c^5}. \tag{3.55}$$

The explicit mass-containing term can be expressed from this equation. By making basic rearrangements, the term can be placed on the left-hand side and denoted as *chirp mass* $\mathcal{M}_{\text{c}}$

$$\mu^{3/5}M^{2/5} = \left(\frac{5}{3}\right)^{3/5}\frac{c^3}{8G}\dot{\Omega}^{3/5}\Omega^{-11/5}. \tag{3.56}$$

The chirp mass can be written in terms of the two masses of the bodies in the system used, for example:

$$\mathcal{M}_c = \mu^{3/5} M^{2/5} = \frac{(m_1 m_2)^{3/5}}{(m_1 + m_2)^{1/5}}. \tag{3.57}$$

The masses of the two bodies can be obtained through observation alone, as this calculation has demonstrated. The calculation of chirp mass and the two masses from a measured signal using a mathematical model is a core subject of this thesis, so this observation is of great significance (pun very much intended).

Following the implementation of the chirp mass as a canonical quantity, the chirp can be defined as a rapid increase in frequency, i.e., $\dot{f}$. In accordance with equation (3.55), it is imperative to acknowledge that the frequency is half that of the GW, given that there are two peaks during an orbit. The angular frequency is therefore $\Omega = \pi f$ and not $2\pi f$. By rearranging the equation and applying the aforementioned substitutions, the following equation is obtained:

$$\dot{f} = \frac{96}{5} \frac{c^3}{G} \frac{f}{\mathcal{M}_c} \left(\frac{G}{c^3} \pi f \mathcal{M}_c \right)^{8/3}. \tag{3.58}$$

Integrating the equation (3.55) such as

$$\int \frac{\mathrm{d}f}{f^{11/3}} = \frac{96}{5} \frac{c^3}{G} \frac{1}{\mathcal{M}_c} \left(\frac{G}{c^3} \pi \mathcal{M}_c \right)^{8/3} \int_t^{t_{\mathrm{coal}}} \mathrm{d}t \,. \tag{3.59}$$

The frequency diverges at a finite value of time. This time can be labelled as the time of coalescence and denoted as t_{coal}. In terms of the time remaining to t_{coal}, the frequency of a GW is

$$f(t) = \frac{1}{\pi} \left(\frac{c^3}{G \mathcal{M}_c} \right)^{5/8} \left[\frac{5}{256 \left(t_{\mathrm{coal}} - t \right)} \right]^{3/8}. \tag{3.60}$$

Following a series of algebraic operations, the following expression is obtained by inserting the (3.58) and frequency (3.60) into (3.43):

$$\frac{\dot{R}}{R} = -\frac{2\dot{f}}{3f} = -\frac{1}{4 \left(t_{\mathrm{coal}} - t \right)}. \tag{3.61}$$

which, after integrating the radius R with respect to time, results in the following equation:

$$\int_{R_0}^{R} \frac{\mathrm{d}R}{R} = -\int_{t_0}^{t} \frac{\mathrm{d}t'}{4\left(t_{\mathrm{coal}} - t'\right)}, \quad \text{that is} \quad R(t) = \left(\frac{t_{\mathrm{coal}} - t}{t_{\mathrm{coal}} - t_0}\right)^{1/4}. \tag{3.62}$$

The R_0 is the value of the radius at the initial time t_0. This indicates that, following a protracted period of relatively uninterrupted decline in radius R, a phase of rapid descent ensues, wherein the approximation of a quasi-circular orbit becomes invalid. It is also possible to express the mass of a chirp via the equation (3.58), for example:

$$\mathcal{M}_{\mathrm{c}} = \frac{c^3}{G}\left(\frac{5}{96}\pi^{-8/3} f^{-11/3} \dot{f}\right)^{3/5}. \tag{3.63}$$

Substituting this into the angle-independent part of either equation (3.53) or (3.54) will yield the desired scaling amplitude. After rearranging and denoting the general distance R to the luminosity distance D, the scaling amplitude assumes the following form:

$$h_0 = \frac{4}{D}\left(\frac{G\mathcal{M}_c}{c^2}\right)^{5/3}\left(\frac{\pi f}{c}\right)^{2/3}. \tag{3.64}$$

In this lowest Newtonian approximation, the amplitudes depend on the masses of the two bodies of the two bodies of the system solely through the chirp mass. By re-arranging the amplitude equation (3.64) so that the luminosity distance D is placed on the left-hand side, the following equation is obtained:

$$D = \frac{4}{h_0}\left(\frac{G\mathcal{M}_c}{c^2}\right)^{5/3}\left(\frac{\pi f}{c}\right)^{2/3}. \tag{3.65}$$

It is evident that the luminosity distance can be ascertained through observation. This is a useful tool for measuring distances in astronomy.

The amplitude of the emitted GWs is contingent on the angle between the line of sight and the axis of angular momentum; the

formula for the amplitude incorporates angular factors of first order. The relative strength of the two polarisations is also contingent on the angle. In the case of three (or more) detectors observing the same signal, it is possible to reconstruct the full waveform and deduce details about the orbit of the binary system.

PART II

ANALYTICAL SECTION

In this section, the analysis of the GW data will be presented. The initial chapter delineates the techniques and formalism employed in the analysis. The following chapters are each dedicated to a specific event and contain a comprehensive analysis, accompanied by explanatory notes and results, with pertinent information regarding the event. The analysis involves the cleaning of the data from the LIGO detectors. Subsequent to this, the data will be divided between the two detectors, and an optimal model will be fitted to obtain the masses m_1 and m_2. The modelled data will be accompanied by residuals, which will demonstrate the degree to which the model aligns with the original data. The scripts/codes used for this analysis follow a consistent pattern, with a change of parameters based on the event itself. The code for GW150914 will serve as an example, with all of the tweaks in the following observations mentioned in the text. The remaining scripts and codes can be found in the Appendix A.3.

4 Introduction to signal processing

The "big three" of this analysis are GW150914, GW170814, and GW170817. The primary reason for this is that they were used in the bachelor's thesis (Hergetová 2024). Implementing them provides an opportunity to compare the analytical techniques used. Also, these are the detections with which everyone is familiar in the context of GW. In addition to the "big three", GW231123 will also appear as it is a new addition to the "more intriguing" detections. The primary objective is to ascertain the masses of the components involved in the merger. An additional goal is to acquire the chirp masses of all detections.

4.1 PyCBC

PyCBC (Nitz et al. 2024) is a Python software package that depends on a Linux-centred compiled scientific software stack. It was developed for the analysis of GW data. This is more than a solid package; it is an open-source resource that allows the community to contribute their models or those that are known but not yet implemented. PyCBC was first used in the initial detection of GW, namely for GW150914. Since then, it has gained popularity as a Python-based analytical tool. This software is highly versatile, as it is capable of analysing raw data to its final form while simultaneously implementing astrophysical parameters of countless mergers. In this thesis, this will function as the primary tool, utilised in all aspects of the analysis, from the initial detection of the signal to determining chirp mass and the masses of each component.

4.1.1 Installation process

The installation process was executed on a Windows computer; however, this resulted in a number of complications. As previously mentioned in the introduction, despite its Python foundation, PyCBC utilises LALSuite (LIGO Scientific Collaboration et al. 2018), a C-based component. LALSuite performs optimally on Linux; therefore, the most suitable approach to ensure functionality was to install WSL (Windows Subsystem for Linux). This knowledge facilitates a rel-

atively straightforward installation process. The fundamental steps involved in the implementation of packages are the creation of a virtual environment and the installation of the packages in this environment. Following the initial installation of LALSuite, the next step involved the installation of PyCBC.

4.2 Used waveform

The central objective of this thesis is to accurately (within the scope of a master's education) assess the chirp mass and the two distinct masses of the objects in a binary system. The PyCBC contains a wide selection of waveforms, so the key is to select the most appropriate one for the analysis. There are two main types:

1. *Time-domain waveform* (*TDW*): The strain (or, as labelled in (3.64), scaling amplitude) is a function of time $h(t)$.

2. *Frequency/Fourier domain waveform* (*FDW*): The strain is a function of frequency $\tilde{h}(f)$.

Based on the names alone, the most appropriate choice is the TDW. The data to be analysed will be the time evolution of the GW that was detected. As previously stated, a multitude of models and waveforms are available, thus enabling the categorisation of TDWs into additional subcategories, including Post-Newtonian Taylor TDWs, TD phenomenological waveforms, effective one-body waveforms, and specialised waveforms for objects exhibiting large eccentricity or spin. The one chosen for this analysis is the effective one-body approximation. Regrettably, this thesis was unable to encompass all the subtypes of the waveforms, given that their description is quite extensive.

4.2.1 Effective one-body waveform (EOB)

This waveform is predicated on the same name formalism. The concept was initially proposed by two French scientists, Alessandra Buonanno and Thibault Damour (Buonanno and T. Damour 1999). Later in 2008, Thibault Damour also published Introductory lectures on this topic (Thibault Damour 2008), which will be used to support all claims in the following text.

Definition

The EOB is an analytical formalism designed to describe the dynamics and GW emission of a coalescing binary system, that is, black holes or neutron stars, in general relativity. It is important to note that the full waveform is modelled, including the inspiral, the merger, and the ring-down. The approach is based on mapping the two-body problem, which is often complex to analyse, to a single effective particle moving in a modified external spacetime geometry that is equivalent and easier to analyse.

Motivations for using EOB formalism and its advantages

This method is chosen because it is essentially the "3-in-1 shampoo" of analysis. As previously mentioned, the model provides extensive physical coverage by describing the dynamics and GW emission of the studied system, capturing all phases of the system [1]. Consequently, the method provides highly precise values for physical properties, as the entire data waveform contributes to the analysis.

It is also quite versatile, as is evident in its ability to function effectively in both general and extreme scenarios. The EOB formalism has been demonstrated to be effective in a range of applications, including systems with equal-mass and extreme-mass ratio, as well as high and low spins, and even eccentric and quasi-circular orbits. (It should be noted, however, that the formalism was primarily developed for quasi-circular orbits. This is a highly advantageous method for the analysis of GWs, given that the identity of the emitting system is unknown.

Principle

The EOB approach comprises three main ideas:

1. *A description of the Hamiltonian part of the BBH (Binary Black Hole) system's dynamics*

   The Hamiltonian represents the motion part that is controlled by gravitational interaction without energy loss. It describes

1. This addresses the issue encountered in the basic model of the preceding thesis (Hergetová 2024), in which the ringdown phase is not incorporated (20-30% relative error in masses)

how the system's position and momentum change over time under purely gravitational, conservative forces (relativistic gravitational attraction, including high-order post-Newtonian (PN) connection). By modelling the conservative part, the EOB formalism represents the orbital evolution parameters (frequency, radius, etc.) up to the point where the dissipative forces take over, enabling a detailed understanding of the BBH system during the inspiral phase.

2. *An expression for the radiation-reaction part of the dynamics*

   This part accounts for the energy and angular momentum lost due to the GW emission. This loss results in a gradually shrinking orbit and an increase in orbital frequency. In the EOB formalism, radiation reaction is represented as a force term that primarily affects angular momentum. Bluntly speaking, the GWs "carry it away". To model this, the EOB formalism uses an expression based on PN results that involves the GW energy flux.

   Specifically, the force $\hat{F}_\varphi$ is obtained from the GW energy flux radiated to infinity. This flux is expressed as a PN-based Taylor series $\hat{F}^{\text{Taylor}}(v)$ where v is the orbital velocity, which is related to the angular velocity Ω. To acquire more accurate results, the Taylor series is re-summed by the Padé approximation (an alternative to polynomial approximation that can approximate a function by using rational polynomial functions (mykd 2021) for analytical functions). This leads to an explicit form of the radiation-reaction force in the equation of motion that is

$$\hat{F}_\varphi = -\frac{32}{5}\,\nu\,\Omega^5 r^4 \hat{F}^{\text{resummed}}(v_\varphi), \tag{4.1}$$

   where the ν is the symmetric mass ratio, r is the separation scaled by GM, Ω is the orbital angular velocity, and the $\hat{F}^{\text{re-summed}}(v_\varphi)$ is the re-summed GW flux function. Simply put, the expression of the radiation-reaction part in the EOB combines the PN theory and the advanced Padé technique.

3. *A description of the GW waveform emitted by a coalescing system*

   This means the EOB formalism involves modelling the entire signal produced as two objects (now illustrating the real event, not the effective approach), inspiral, merge, and settle into a final object. The GW waveform is derived using high-order (PN) expanded results, which were obtained over many years by other research teams. These results provide highly accurate approximations for the GW amplitude and phase during the early inspiral phase.

   As mentioned in idea number two, the EOB formalism does not use the raw Taylor expanded PN series but applies the Padé resummation, securing a form that converges better; therefore, it provides better and closer results to the merger. The modelling also involves matching the inspiral waveform to the plunge and merger phases, which are its smooth continuation. Lastly, the ring-down is modelled as a relaxation of the merger remnant as a superposition of quasi-normal modes of the final object, providing a consistent waveform at the end of coalescence.

   These steps produce a full waveform incorporating all stages of binary coalescence. This can be directly compared with highly accurate numerical relativity (NR) results. The lessons (Thibault Damour 2008) contain references to the "recent studies" (late 2000's studies) that have surprisingly large agreement between EOB waveforms and NR simulations.

4.2.2 Used models

The first model employed was `SEOBNRv4_opt`. The name can be interpreted as *Standard Effective-One-Body Numerical Relativity*. This model has been developed specifically for spinning, non-precessing binary black holes. This is ideal for the events GW150914, GW170814, and GW231123. It has been fine-tuned to a substantial array of numerical relativity simulations, encompassing diverse mass ratios and spins, thereby ensuring reliable predictions even for extreme scenarios. Furthermore, the model successfully reproduces the late stages of black hole mergers, where strong gravitational fields prevail, with a high degree of accuracy. Lastly, the reduced-order modelling component

allows rapid waveform generation. The `_opt` part stands for *optimised*. This process is designed to facilitate more rapid analysis by examining data in bulk rather than in individual points (Bohé et al. 2017).

The second model is `TEOBResumS`. This model is used for a binary neutron star merger (BNSM) GW170817. The name can be interpreted as *Tidal Effective One Body Resum Spin-aligned*. This model is a calibrated analytical waveform that accurately captures the complex phenomena present in BNSM. Such waveforms include tidal deformation and spin effects. This makes the model well-suited for this analysis (Nagar et al. 2018).

4.3 Optimisation

4.3.1 Differential Evolution (DE)

Once the models have been selected, a search tool will be required. As is standard practice with these models, precise information about the system is entered to generate a fitted model. In this analysis, the information is derived from the model. It is therefore the ideal time to implement optimisation strategies.

Definition

DE is a parallel, direct-search optimisation method that has been designed to minimise continuous, non-linear, and non-differentiable functions. The method operates on a population of candidate solutions (parameter vectors) and iteratively improves them using their differences. The core concept is to generate new candidate solutions by adding weighted differences of randomly selected candidate vectors to existing vectors to ensure exploration.

The starting point is a randomly generated population of parameter vectors within predefined bounds. In the scenario of this analysis, the method works in 4D because it is meant to find the best results in both masses, scaling of the model, and time offset from the merge time (which can be due to the distance between detectors). For each candidate vector, DE creates a trial vector by combining other vectors in the population.

The trial vector undergoes a crossover process with the original candidate, exchanging components based on a pre-determined crossover probability, with the aim of producing a more diverse range of results. If the trial vector yields a lower objective function value than the original, it replaces the original candidate in the population. This process is repeated over multiple iterations (Storn and Price 1997).

Motivation

The DE was not the initial choice for this analysis. Many trials and errors were conducted with various methods, some of which might have been faster or better in other ways, but the DE met all the desired requirements. These requirements are:

1. *Global search*

   A global search is important as it is crucial to match the right minimum. If a local search were used, a very accurate initial estimate would be necessary. The objective of this analysis is to determine masses from the ground up, with the initial guess being an interval of possible masses for the system. This is later narrowed down to a smaller interval to enhance the precision of the search. Local search would be an appropriate strategy for BNS, as neutron stars are likely to have a mass of around $1.4\,M_{\odot}$. However, for BBH, this approach would not be very practical.

2. *Reliability*

   It is important to use a method that has a low error rate. The analysis of one event is run multiple times, where (as previously mentioned in point 1) the initial interval is gradually reduced step-by-step to ensure the highest possible accuracy. The process functions more seamlessly when the method does not encounter "fake" values or converge to unusual outcomes.

3. *Derivative-free*

   To be transparent, methods with derivatives would be counterproductive. Differentiation is not required in this instance; therefore, there is no need to implement it.

4. *Speed*

   The faster, the better. However, if the run time for optimisation is less than 15 minutes, it is still a very good option for this analysis.

Used strategy

For this analysis, the `best1bin` function from the `scipy.optimize` module was utilised, as it is widely regarded as a reliable starting point. In this strategy, two members of the population are randomly selected. Their difference is used to mutate the best member:

$$b' = x_{r_1} + F \times (x_{r_2} - x_{r_3}), \tag{4.2}$$

where x_{r_1} is the best member, F is a mutation parameter, and x_{r_2} and x_{r_3} are random members. This equation demonstrates that the algorithm is attempting to identify the smallest discrepancy, which suggests that the population is in proximity to the correct answer. If the difference were significant, it would mean that the population is still highly dispersed.

The algorithm now has both the original candidate and the newly mutated b' candidate. It then selects a random number within the interval $[0, 1)$. This is compared to a recombination constant (RC). In the absence of an explicit value, the `scipy` function will automatically set the value to 0.7. If the random number is smaller than the RC, the value from b' is selected as the best option. If not, the value is selected from the original. The next step is to construct a trial vector. To ensure that the trial vector is not the same as the original, the algorithm will randomly select at least one parameter from the b set.

A comparison is made between the original and the trial vector. The most accurate one is then selected and used as the original. If it were to outperform the overall best, it would naturally replace it (Jones et al. 2001–; Virtanen et al. 2020).

5 GW150814

The GW150914 event, as indicated by its title, occurred on 14 September 2015 at 09:50:45 UTC (Coordinated Universal Time). The detected GWs were of a binary black hole merger (BBHM) origin. The signal detected was consistent with the predictions of general relativity for a binary system. In this detection, the theory of general relativity was confirmed. This momentous event signalled the start of a new era in the study of astronomy, contributing to the advancement of humankind (B. P. Abbott et al. 2016).

5.1 Data preparation

The data preparation process was straightforward, as PyCBC includes all the essential steps in a small number of convenient functions. The `PyCBC` project has a GitHub repository (Nitz, Harry, et al. 2024) that contains tutorials for the various steps of the analysis, enabling users to follow them to clean the data.

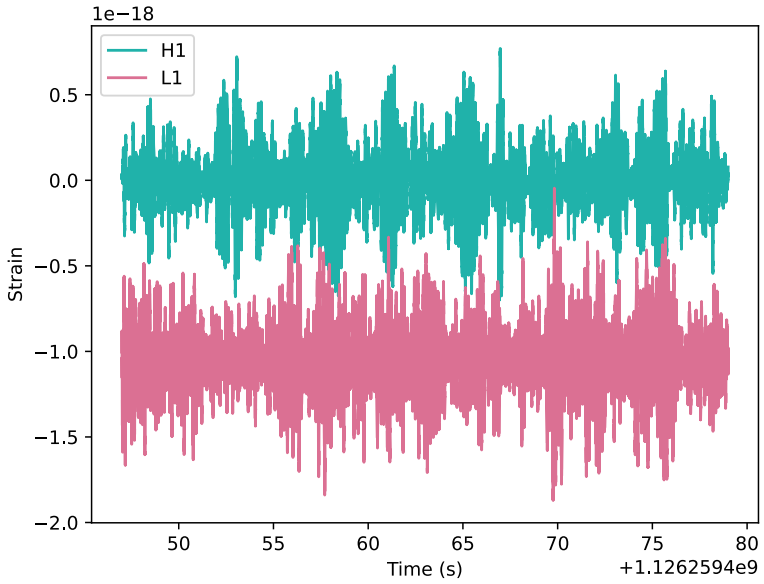

Figure 5.1: Raw GW150814 data.

Cleaning data is done in two steps:

5.1.1 Whitening

Whitening is an essential step in the process. In this procedure, a power spectral density is generated (from now labelled PSD). PSD is a measure of the distribution of power (or variance) across different frequencies in a time-series signal. It is typically represented by a curve resembling a "U". This showcases the detector noise and its three parts: seismic noise, thermal noise, and quantum noise (from left to right). The raw data is then divided by the square root of the PSD. This process ensures that the noise becomes uniform; that is to say, the frequencies are rendered equivalent in terms of perceived loudness. PSD then looks flat, and the data are prepared for the subsequent stage. For comparison, Figures 5.2 and 5.3 show the before and after of the PSD, and 5.4, which presents the resultant whitened data. The PSD is found to be flat, in accordance with predictions, and the data appear to be uniform (within the bounds of possibility) without large "fangs/teeth".

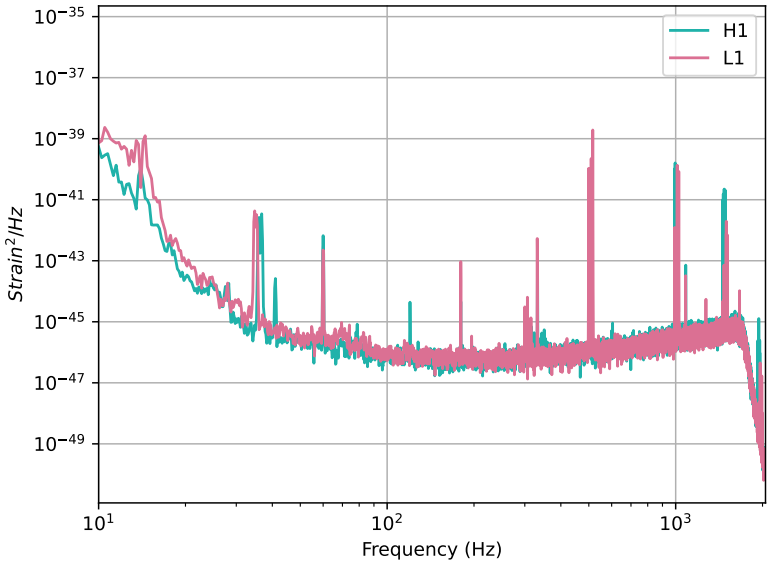

Figure 5.2: PSD GW150814 of data.

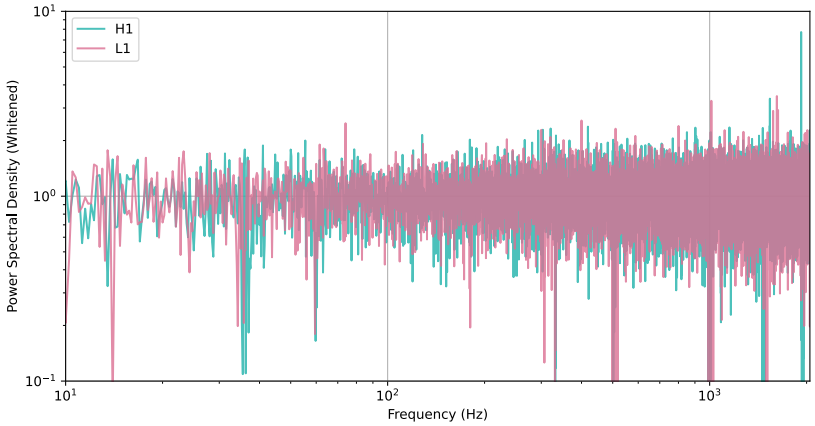

Figure 5.3: Whitened PSD of GW150814 data.

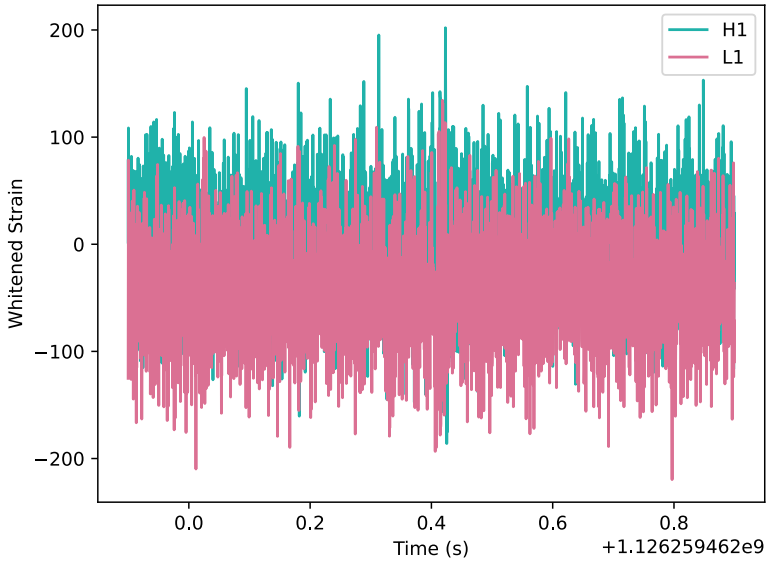

Figure 5.4: Whitened GW150814 data.

5.1.2 Bandpassing

As previously stated, there are three primary categories of noise: seismic noise, thermal noise, and quantum noise. Each of these is characterised by a distinct frequency. The function of bandpass filtering

is to eliminate the noise that is interfering with the signal. At lower frequencies, the issue is seismic activity, and at higher frequencies, quantum "shot noise" is a concern. The bandpassing function is utilised to identify the frequency range within which the GW signal is anticipated. The range is dependent on the type of detection in question, whether it is BNS or BBH, and the object's mass. This will demonstrate the velocity at which the objects orbit each other before collision. For GW150914, the high-pass filter is 30 Hz and the low-pass one is 250 Hz. As these are standard filters for events with typical characteristics, they provide a solid starting point (and, in this case, a suitable option to use until the end). As demonstrated in Figure 5.5, the whitened and bandpassed data are displayed, and in Figure 5.6, the merger is zoomed in on.

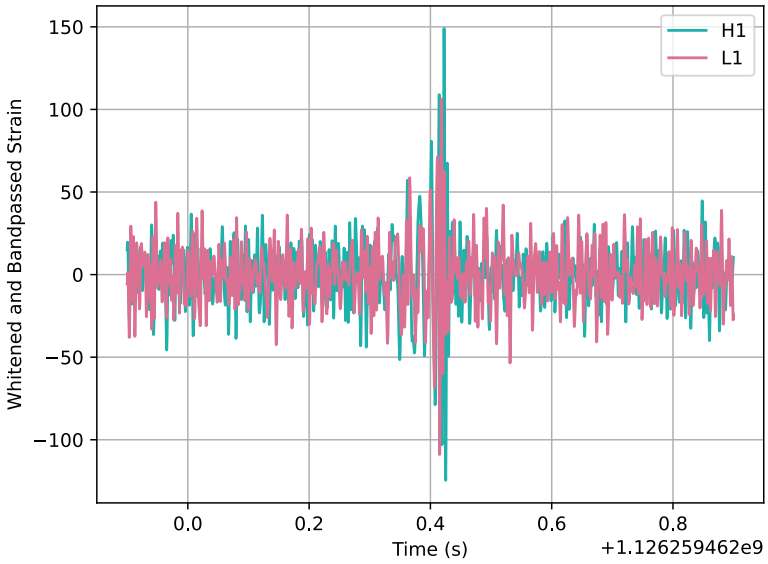

Figure 5.5: Cleaned up GW150814 data.

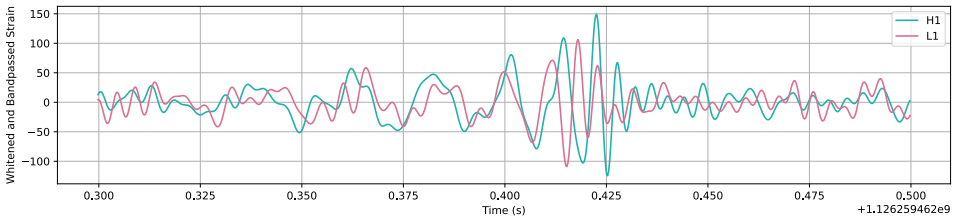

Figure 5.6: Zoomed in clean GW150814 data.

5.2 Modelling of the data

5.2.1 Match Function

The match function is coded to determine the most fitting matches. The algorithm provides estimates for the object masses and evaluates the similarity between these and the actual data. Firstly, the parameters are defined as masses $m1$ and $m2$, time offset, and scale. As previously referenced in the 4.3.1. Subsequently, the function `get_td_waveform` from the PyCBC software is utilised to generate a theoretical GW template that the masses will be entered into. As previously stated in 4.2.2, a `SEOBNRv4` model is used as this is a BBHM. The model function also includes a parameter, denoted as `delta_t = dt`, where `dt = zoom_h1.delta_t`. This is simply a method of indicating to the model where it should "place" itself in time. In this instance, the modelling is limited to a segment of the data around the merge, as it would be problematic to ascertain the precise positioning of the data on a larger scale. The final parameter is simply a lower frequency, which is equivalent to the lower bandpass filter. The code is as follows:

```
# MATCH FUNCTION
def match_score(params):
    m1, m2, time_offset, scale = params

    try:
        hp, _ = get_td_waveform(
            approximant="SEOBNRv4",
            mass1=m1, mass2=m2,
            delta_t=dt, f_lower=30
        )
```

Listing 5.1: Beginning of match fucntion.

The match function contains code that validates the model's alignment with the data. The model's largest peak is attempting to locate the data's largest one, as this would ensure that the real and theoretical plunge and merge align with each other. The final segment of the match function involves the calculation of the Least Squares (LS). The model is subtracted from the data; the result at each point is squared (in order to remove negative numbers), and the sum of these values is then calculated. If the model is a perfect match, the subtraction leaves almost nothing but zero, resulting in a very low score; therefore, it is an excellent match, as the difference is minimal.

5.2.2 Optimisation

To optimise the search, the following code is employed:

```
bounds = [
    (20, 50),          #mass1 range
    (15, 45),          #mass2 range
    (-0.05, 0.05),     #time offset range
    (-2.0, 2.0)        #scale range
]
result = differential_evolution(
    match_score,
    bounds,
    strategy='best1bin',
    popsize=100,
    tol=1e-15
)

best_m1, best_m2, best_time, best_scale = result.x

print(f" Best masses are m1: {best_m1:.2f} and m2: {
    best_m2:.2f} + also time offset: {best_time:.4f} and
    scale: {best_scale:.2f}")

m1_f, m2_f = (best_m1, best_m2) if best_m1 >= best_m2
    else (best_m2, best_m1)
```

Listing 5.2: Starting optimalisation bounds and function.

The bounds indicated are from the initial run. It is customary for the m_2 to be smaller, which explains why the initial mass interval remains unchanged but is simply shifted to lower values. The masses are defined in solar masses, as implied in the text, although not explicitly

stated. The time offset is in seconds, and the scale is dimensionless. The time offset is measured in seconds, and the scale is dimensionless. Following several iterations, the values will converge on a single value, allowing the intervals to be narrowed at a later stage. The final bounds are as follows:

```
#H1
bounds = [
    (35.3, 35.7),           #mass1 range
    (30.1, 30.5),           #mass2 range
    (0.0024, 0.0028),       #time offset range
    (0.95, 0.98)            #scale range
]

#L1
bounds = [
    (35.2, 35.5),           #mass1 range
    (29.9, 30.3),           #mass2 range
    (0.0025, 0.003),        #time offset range
    (-0.88, -0.83)          #scale range
]
```

Listing 5.3: Final bounds for GW150914.

In the context of the `differential_evolution`, the match function, bounds, and strategy previously referenced in the text are utilised. It also contains the function `popsize`; this spawns a population of 100 random guesses, where the lowest-scoring guesses from the match function survive and are used in subsequent calculations, as was likewise mentioned in 4.3.1. Finally, `results.x` are the results obtained from the optimisation process.

5.2.3 Final assembly

Once the best parameters have been identified, they are again plugged into the model and aligned with the data. The residuum is calculated by subtracting the model from the data. In order to facilitate the modelling process, the data were divided into two segments, H1 and L1, and modelled independently. This decision was made to subsequently calculate the mean value of both masses and the chirp mass of the system. This approach enables the use of a statistical deviation. Evidently, a deviation can be obtained from all of the iterations. However, this is

contingent upon the bounds, which can be calibrated to achieve the minimal possible deviation. This approach ensures a certain degree of fairness in the results.

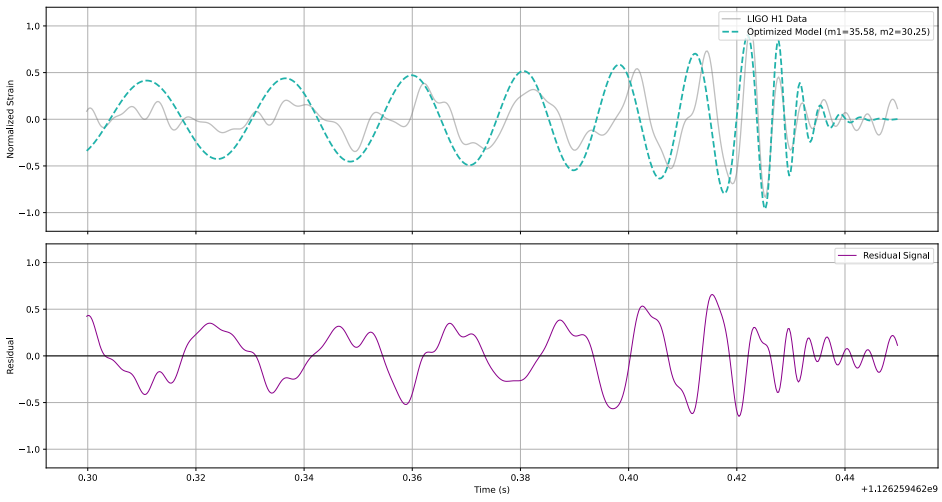

Figure 5.7: *Top:* GW150914 data from Hanford (Washington, US) with optimised model; *Bottom:* Residual signal from modelling GW150914 H1 data.

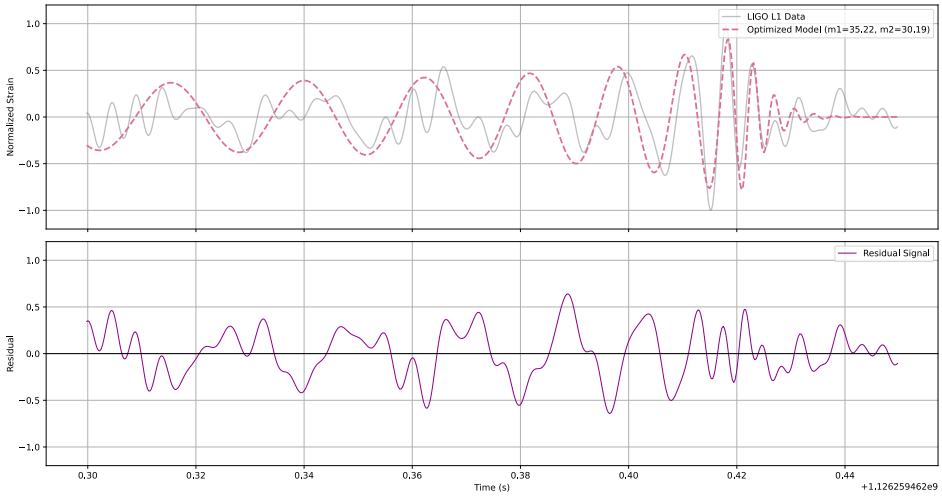

Figure 5.8: *Top:* GW150914 data from Livingston (Louisiana, US) with optimised model; *Bottom:* Residual signal from modelling GW150914 L1 data.

Final models with residuals are depicted in Figures 5.7 and 5.8

5.3 Additional information on data and chirp mass calculation

This section of the code provides insight into the modelling process. The first part of the process is to calculate an "overlap". The overlap is defined as the cosine similarity, as the code shows.

```
#OVERLAP CALCULATION
overlap = np.dot(data_to_plot, model_plot) / (np.linalg.
    norm(data_to_plot) * np.linalg.norm(model_plot))
overlap_percentage = overlap * 100

print(f"Overlap: {overlap_percentage:.2f}%")
```

Listing 5.4: Overlap/Cosine similarity.

When assessing "shape" similarity, a comparison of vectors is the preferred method, given that the GW signal is characterised by noise, even following data filtration. The cosine similarity is a mathematical function that is specifically designed to ignore random noise and to

recognise only the parts of a wave that are in phase with the signal (Tom Krantz 2025). The overlap is a number in the interval $[-1, 1]$, so for clarity, the code converts the result to a percentage. To elaborate further on the significance of the values, 1 signifies complete similarity between the vectors, with their orientations pointing in the same direction. 0 denotes orthogonality, indicating that the vectors are not directionally similar. Finally, -1 indicates that the vectors have opposite orientations.

To calculate the chirp mass, the code first identifies the best resulting masses from the fitting process, and these are then plugged into the equation (3.57).

5.4 Results

Parameters	H1 data	L1 data
Primary mass ($M_\odot$)	35.58	35.22
Secondary mass ($M_\odot$)	30.25	30.19
Chirp Mass ($M_\odot$)	28.54	28.37
Time offset (ns)	2.50	3.00
Scale	0.97	-0.84
Overlap (%)	66.56	61.23

Table 5.1: Results of the analysis and modelling of the GW150914 data

6 GW170814

GW170814 was detected on 14 August 2017 at 10:30:43 UTC. The GWs detected were also from a BBHM source, similarly to GW150914. The detected signal was observed by both LIGO and Virgo detectors. The detected signal was observed by both LIGO and Virgo detectors. The implementation of a network comprising three detectors enhances the sky localisation of the source. This provided the first-ever opportunity to test the nature of GWs' polarisations from the antenna response. This development paved the way for a new class of phenomenological tests of gravity (B. P. Abbott et al. 2017a).

6.1 Data preparation

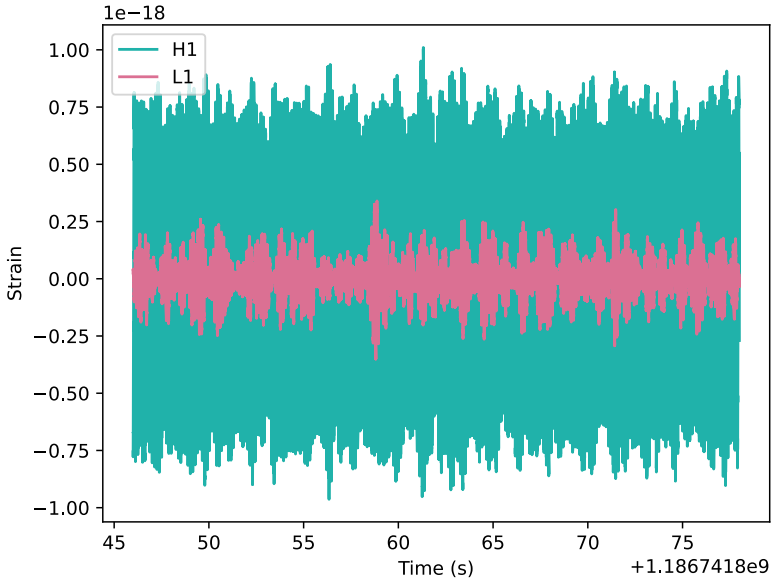

Figure 6.1: Raw GW170814 data.

As outlined in Figure 6.1, the raw data underwent whitening and bandpass filtering. For GW170814, the initial filters were identical to those used for GW150914; however, during the cleaning process, they were adjusted to 20 Hz. The primary motivation behind this decision

was that the initial data appeared to be relatively uninformative and quite flat. Subsequent analysis of the mass values further validated this decision. The ensuing discussion will be expounded upon in the *Results* section 6.3.

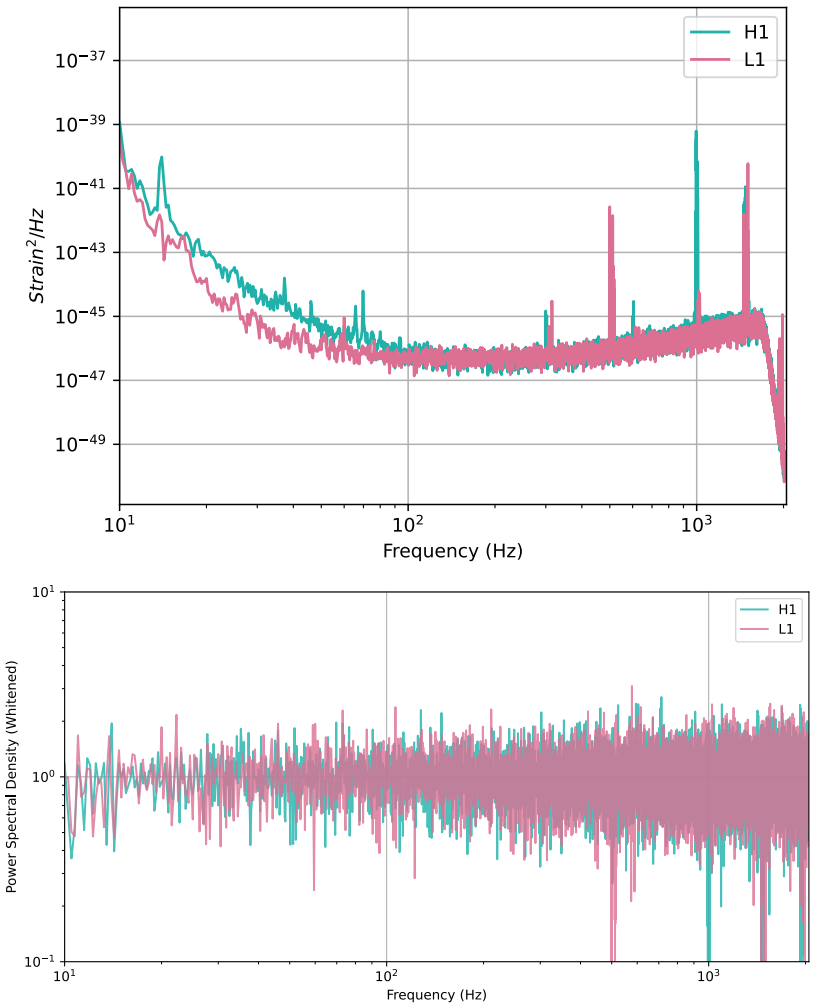

Figure 6.2: PDS of GW170814 data before and after whitening.

As cleaning was explained in chapter 5, the presentation of a graph containing solely whitened data is not necessary, as it is neither visually interesting nor important for the analysis. As illustrated in Figure 6.2,

the change in PSDs is evident. The final data with zoom are presented in Figure 6.3.

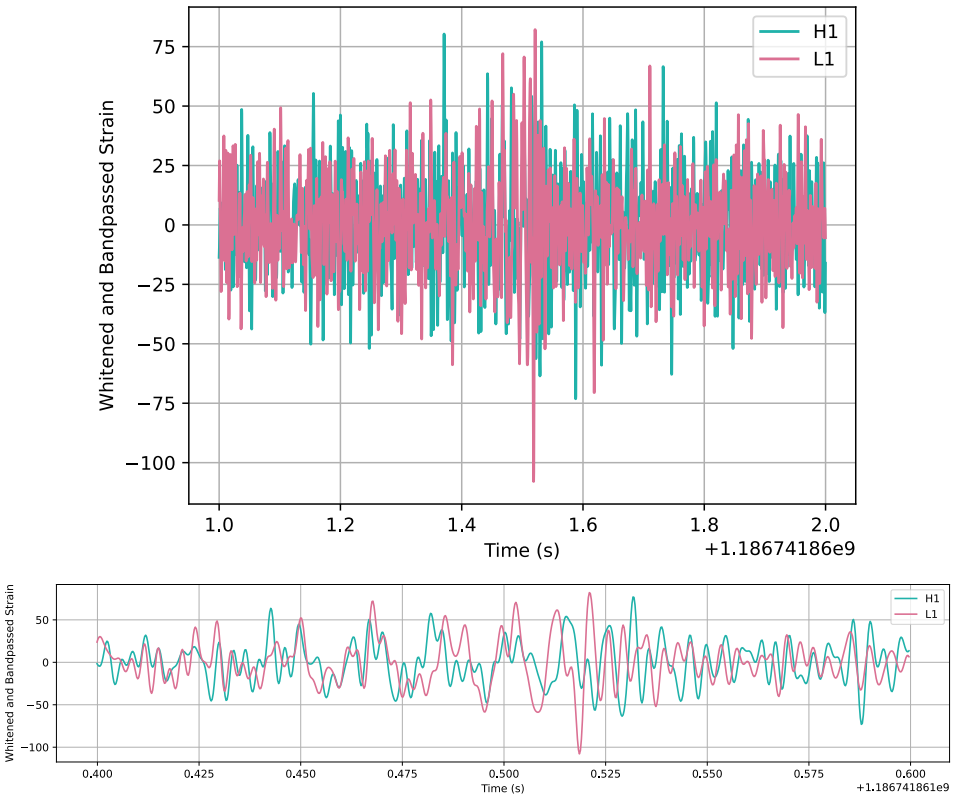

Figure 6.3: Clean GW170814 data and their zoom.

6.2 Modelling of the data

Concerning the modelling of the data, there was no significant plunge or merger element. The data were divided once again, and the same initial bounds were employed as for GW150914. The final bounds, written in the listing below, and the final graphs are depicted in Figures 6.4 and 6.5.

```
#H1
bounds = [
    (30.8, 31.0),           #mass1 range
    (24.8, 25.5),           #mass2 range
    (-0.001, 0.001),        #time offset range
    (-0.95, -0.8)           #scale range
]
#L1
bounds = [
    (30.5, 31.0),           #mass1 range
    (25.0, 25.5),           #mass2 range
    (0.001, 0.005),         #time offset range
    (0.7, 0.75)             #scale range
]
```

Listing 6.1: Final bounds for GW170814.

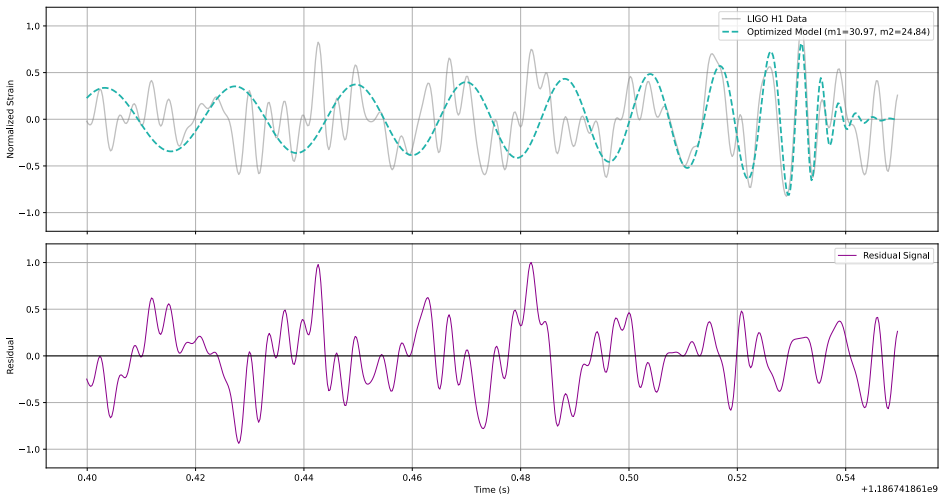

Figure 6.4: *Top:* GW170814 data from Hanford (Washington, US) with optimised model; *Bottom:* Residual signal from modelling GW170814 H1 data.

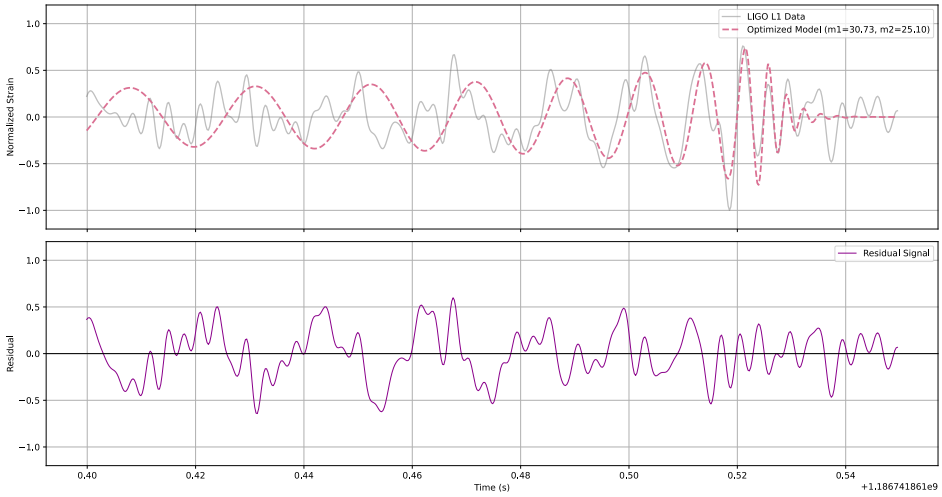

Figure 6.5: *Top:* GW170814 data from Livingston (Louisiana, US) with optimised model; *Bottom:* Residual signal from modelling GW170814 L1 data.

6.3 Results

The results of the analysis are set out in Table 6.1. As previously mentioned, the band-pass filters were adjusted to accommodate the data, as they were initially found to be flat. The flatter appearance of the images when using the base filters can be attributed to the masses. This system is slightly less massive than GW150914, meaning that black holes can get closer before merging, which in turn pushes the peak frequency up a bit.

Parameters	H1 data	L1 data
Primary mass ($M_\odot$)	30.97	30.73
Secondary mass ($M_\odot$)	24.84	25.10
Chirp Mass ($M_\odot$)	24.12	24.15
Time offset (ns)	0.00	3.00
Scale	-0.81	0.74
Overlap (%)	43.93	55.35

Table 6.1: Results of the analysis and modelling of the GW170814 data.

7 GW170817

Another source of data is GW170817. The detection was made on 17 August 2017 at 12:41:04 UTC and was accompanied by a gamma-ray burst, specifically a sGRB (short gamma-ray burst). The gamma-ray burst was detected independently of the GWs by the Fermi and INTEGRAL satellites. It was only during the subsequent data analysis that these two events were linked. The observed source was identified as a binary neutron star merger (BNSM). The observed source was identified as a binary neutron star merger (BNSM). The detection findings confirmed a specific correlation between GWs from NS-NS systems and short gamma-ray bursts (B. P. Abbott et al. 2017b).

7.1 Data preparation

In the case of GW170817, the preparation process is particularly challenging. The data exhibit an instrumental glitch on the Livingston detector. The glitch was so prominent that it was even visible in the raw data. As demonstrated in the previous two chapters, the raw data typically appear to be noise. The raw data are depicted in the Figure 7.1.

Due to the size of the glitch, two different approaches were used. To illustrate the full extent of the data, the high-pass filter was set at 30 Hz, while the low-pass filter was set at 1500 Hz. This ensures that the magnitude of the glitch is preserved. For the data analysis, the high-pass filter was set to 30 Hz and the low-pass filter to 400 Hz. This discrepancy can be attributed to the incompatibility between the glitch's modelling and the employed approach; a dedicated glitch analysis is needed. It appears that the H1 data could be modelled, and therefore the relevant analysis was carried out. As illustrated in Figure 7.3, the flattening of the PDS is executed nicely.

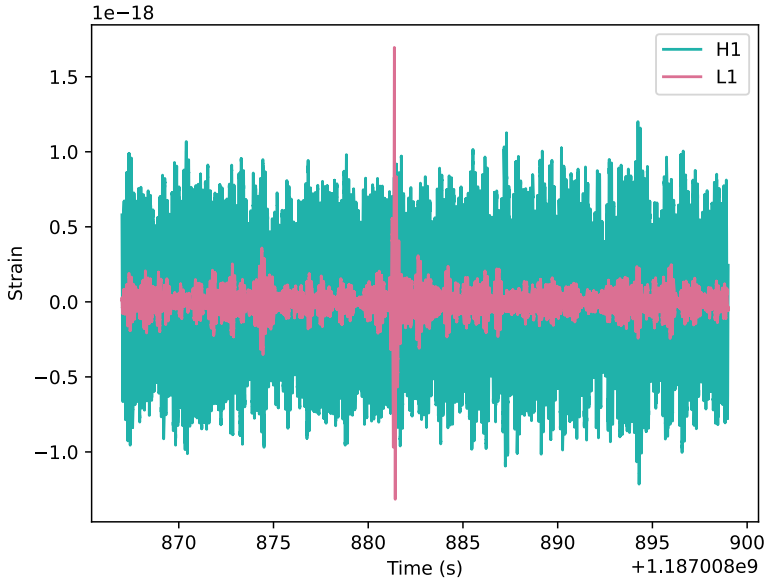

Figure 7.1: Raw GW170817 data.

As illustrated in Figure 7.2, the clean data have been zoomed in. The prominent glitch takes over the data, and only a slight "wiggle" can be seen in other places, as well as in the whole H1 data.

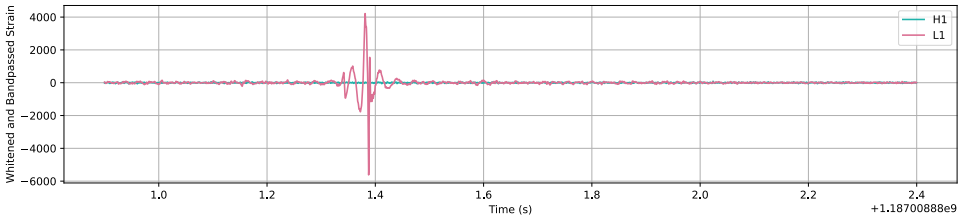

Figure 7.2: Zoomed in clean GW170817 data.

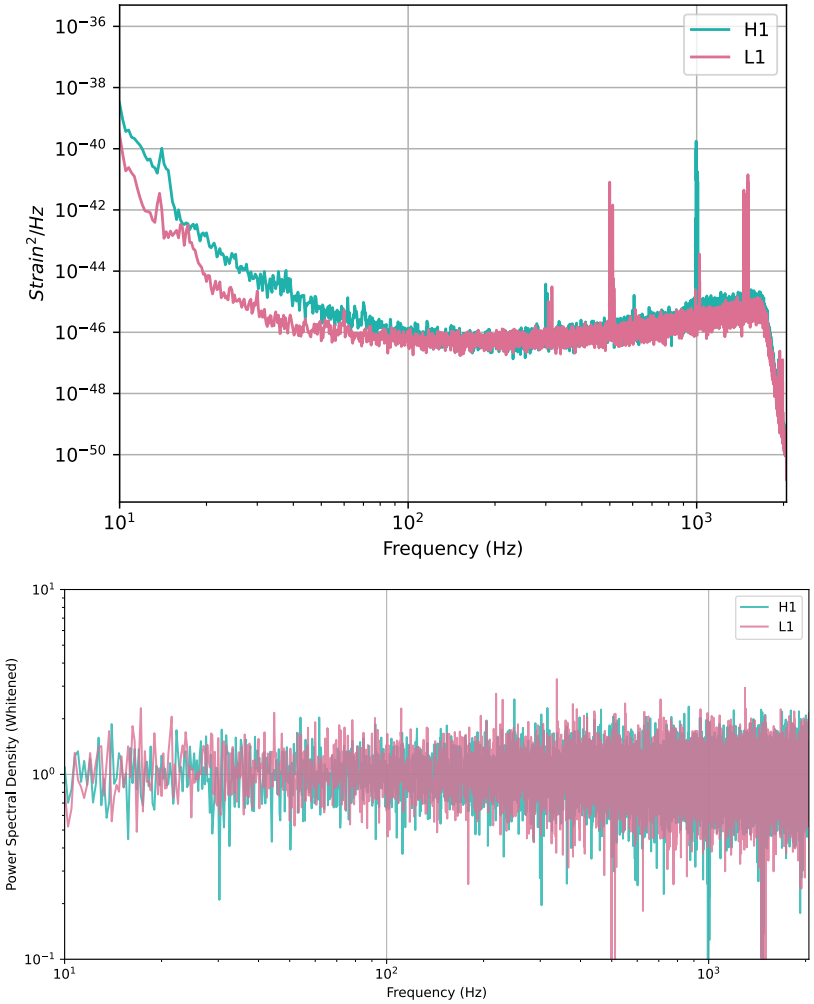

Figure 7.3: PDS of GW170817 data before and after whitening.

7.2 Modelling of the data

As previously stated, only the H1 will be considered for analysis. As this is a BNSM, the initial boundaries differed. It is estimated that the mass of a neutron star is approximately 1.4 $M_{\odot}$. However, for the optimisation to be successful, it is necessary to consider an interval. The initial bounds were selected based on these considerations.

```
bounds = [
    (1.10, 1.60),          #mass1 range
    (1.0, 1.50),           #mass2 range
    (-0.02, 0.02),         #time offset range
    (-2,0, 2.0)            #scale range
]
```

Listing 7.1: Starting bounds for H1 of GW170817.

Following a series of tests, the hypothesis was confirmed, and the primary mass began to oscillate around the $1.4\,M_{\odot}$ value. As anticipated, the secondary mass transitioned to a smaller mass, as the secondary mass should invariably be smaller than or equivalent to the primary mass. The final bounds are as follows:

```
bounds = [
    (1.43, 1.48),          #mass1 range
    (1.25, 1.30),          #mass2 range
    (-0.02, 0.02),         #time offset range
    (0.5, 1.5)             #scale range
]
```

Listing 7.2: Final bounds for H1 of GW170817.

As for the final plot with modelled data and residuals, the outlook is not promising. Despite the initial hypothesis that the H1 data could potentially provide accurate results, this was not the case. The H1 data does not contain a visible plunge and merge that the model could detect. Additionally, upon examination of the residuum, a subtle waveform can be discerned amidst the noise interference. Notably, the model displays a tendency to adhere to the peaks rather than follow the waveform. While the modelled masses do align with the published results, it is evident that this is merely a coincidental convergence. The overlap between these functions is negligible, indicating that the vectors are essentially orthogonal. A more detailed discussion of the subject will be found in the section *Conclusion* 10. The final plot is illustrated in Figure 7.4. The results have been documented in Table 7.1.

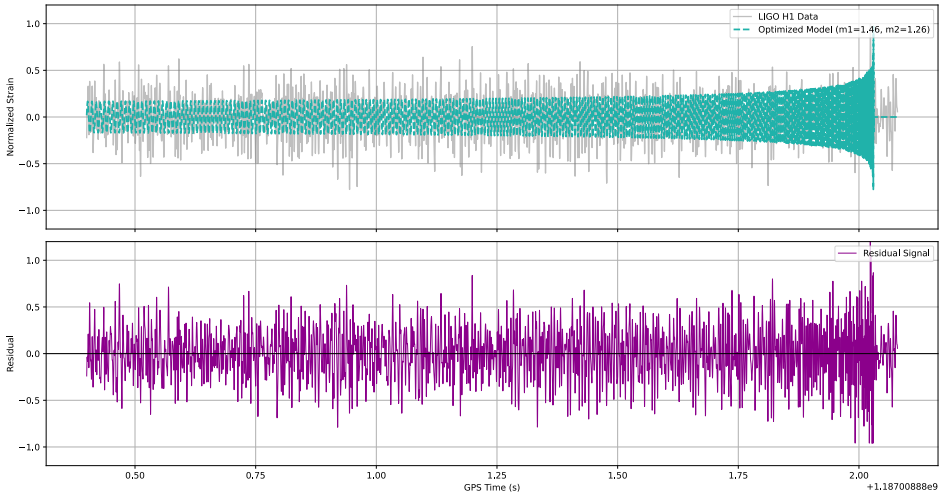

Figure 7.4: *Top:* GW170817 data from Hanford (Washington, US) with optimised model; *Bottom:* Residual signal from modelling GW170817 H1 data.

7.3 Results

Parameters	H1 data
Primary mass ($M_\odot$)	1.46
Secondary mass ($M_\odot$)	1.26
Chirp Mass ($M_\odot$)	1.18
Time offset (ns)	6.10
Scale	1.83
Overlap (%)	1.15

Table 7.1: Results of the analysis and modelling of the GW170817 data.

8 GW231123

The last detection of this analysis is GW231123. The detection from November 23, 2023, is notable for the masses of the binary's components. The GWs originated from binary black holes (BBH), similar to GW150914, yet the masses of the individual components were approximately 100 times the mass of the Sun. The black hole remnant of this merger is estimated to be approximately 200 $M_{\odot}$. This finding indicates that the formation of black holes may not be exclusively attributable to stellar collapses. It is proposed that this mass category of black holes may also form through mergers driven by GWs (Abac et al. 2025).

8.1 Data preparation

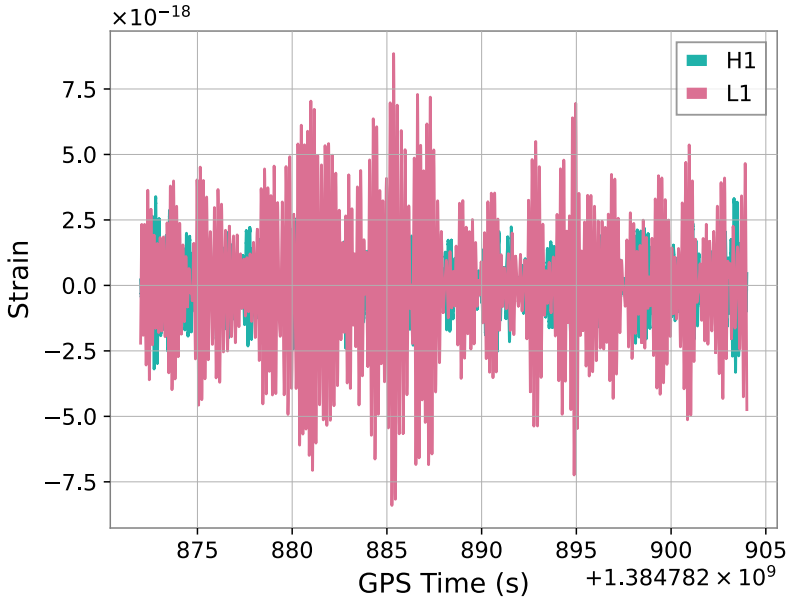

Figure 8.1: Raw GW231123 data.

As this is an unusual detection, the preparation of the data was completed in a slightly different manner. At the time of analysis, the neces-

sary data were not available in PyCBC. Therefore, the data had to be retrieved using `gwpy.timeseries`. This approach necessitated a more extensive analysis due to the longer time required for data import. Fortunately, upon loading, the analysis functioned in the same manner as the preceding analyses. The raw data are depicted in the Figure 8.1.

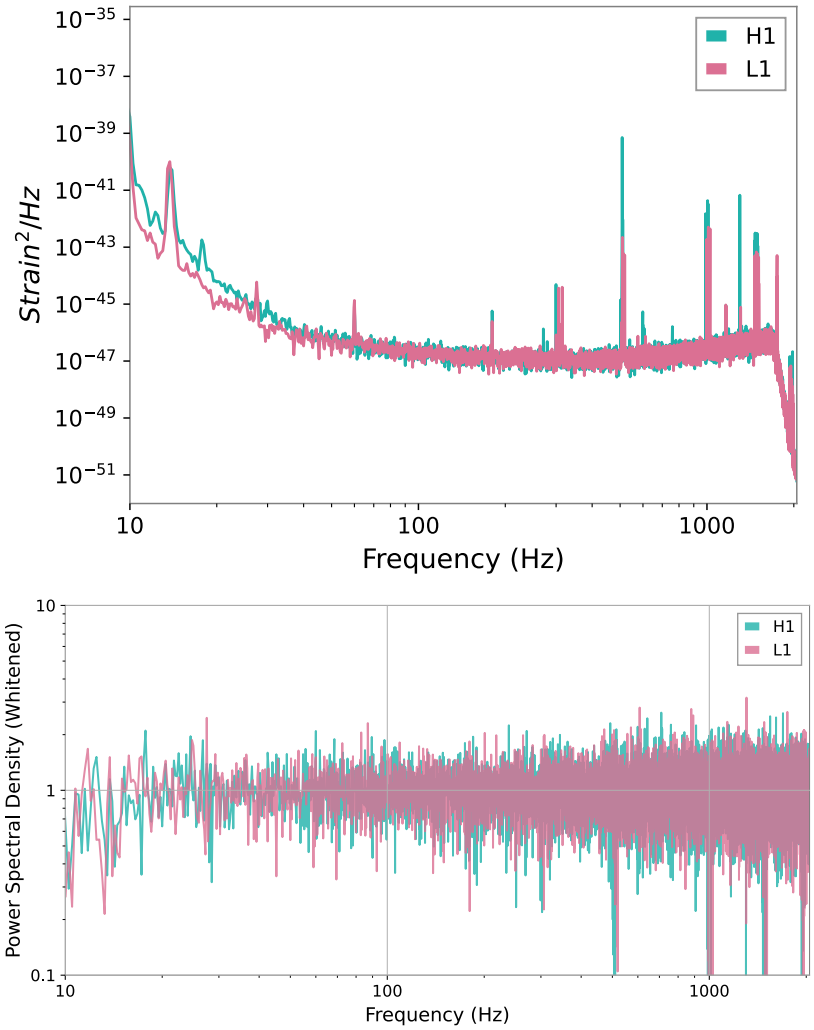

Figure 8.2: PDS of GW231123 data before and after whitening.

This is the most massive merger detected to date; the logic employed in the NSBM GW170817 can be applied to conclude that the

merger happened rapidly, thus requiring a lower bandpass. In this instance, the high-pass filter was determined to be 10 Hz and the low-pass filter to be 150 Hz. This approach ensures that low-frequency components do not become obscured by higher frequencies. In Figure 8.2, there is once again a successful whitening effect of the PSDs.

The clean data and their zoom are depicted in Figure 8.3.

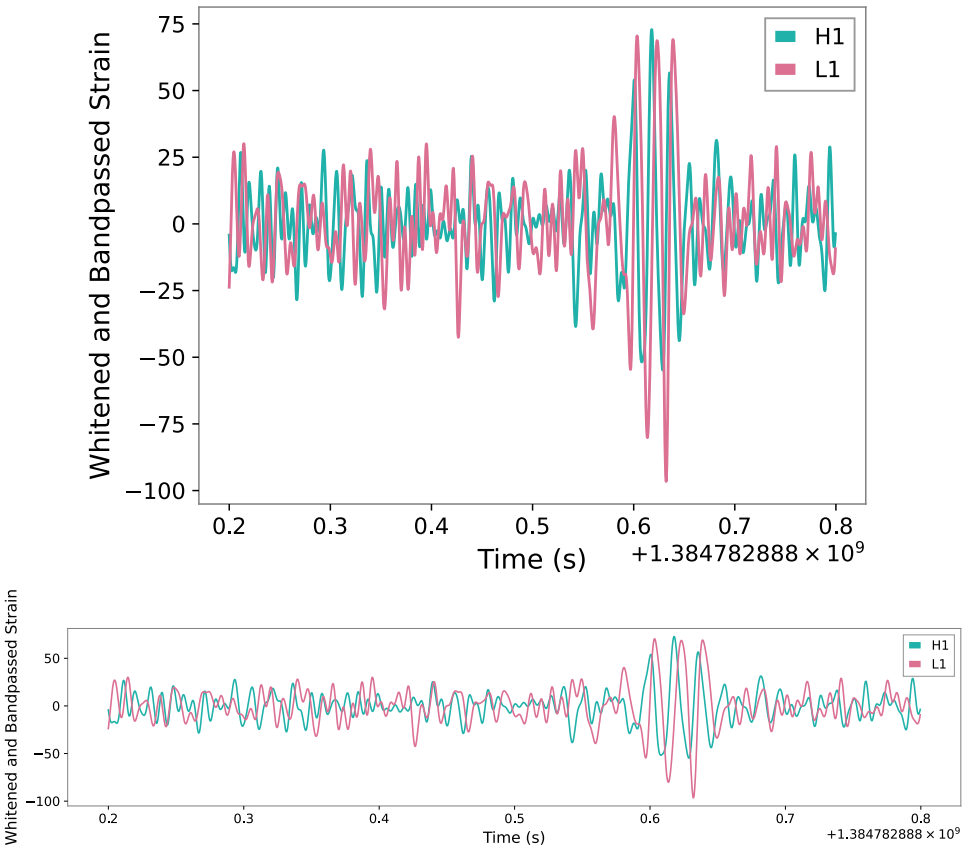

Figure 8.3: Clean GW231123 data and their zoom.

8.2 Modelling of the data

Due to the significant scale of this event, a new starting boundary will be used. The two objects are known as intermediate-mass black holes (IMBHs), with masses ranging from $10^2 - 10^5\, M_\odot$. If this analysis

were conducted with such broad bounds, it would require a significant amount of time. This is the only part of the analysis where the estimate was made using knowledge of the masses being approximately $\sim$ 100 $M_{\odot}$, as obtained from the abstract of a published paper discussing this event (Abac et al. 2025). Before this, the sole source of information was general knowledge obtained at the university during the past years.

With this in mind, the starting bounds were chosen as:

```
bounds = [
    (100, 150),          #mass1 range
    (95, 145),           #mass2 range
    (-0.05, 0.05),       #time offset range
    (-2.0, 2.0)          #scale range
]
```

Listing 8.1: Starting bounds for GW231123.

Following a series of trials, an issue was identified. The model was found to be compatible with only the merger part or the inspiral part, with an overlap typically ranging from 5% to 10%. Consequently, a new approach was adopted: namely, modelling the inspiral and the merger separately to achieve the optimum overlap. It was also necessary to attempt to adjust the bandpassing, since this could potentially cause a problem. However, if the analysis concentrated on the inspiral phase, the model failed to capture the merger. Similarly, when the focus was on the plunge and merge, the peaks were followed more than the inner wave structure present in the inspiral segment. The band-pass filter configuration will therefore remain unchanged. The four modelling attempts are depicted in the Figures 8.4 and 8.5.

```
#H1
bounds = [
    (130, 133),          #mass1 range
    (110, 112),          #mass2 range
    (0.01, 0.015),   #time offset range
    (-0.5, 0.0)           #scale range
]
#L1
bounds = [
    (130, 135),          #mass1 range
    (110, 115),          #mass2 range
    (-0.01, -0.005),   #time offset range
    (0.0, 0.5)           #scale range
```

```
]
```

Listing 8.2: Final bounds for GW231123.

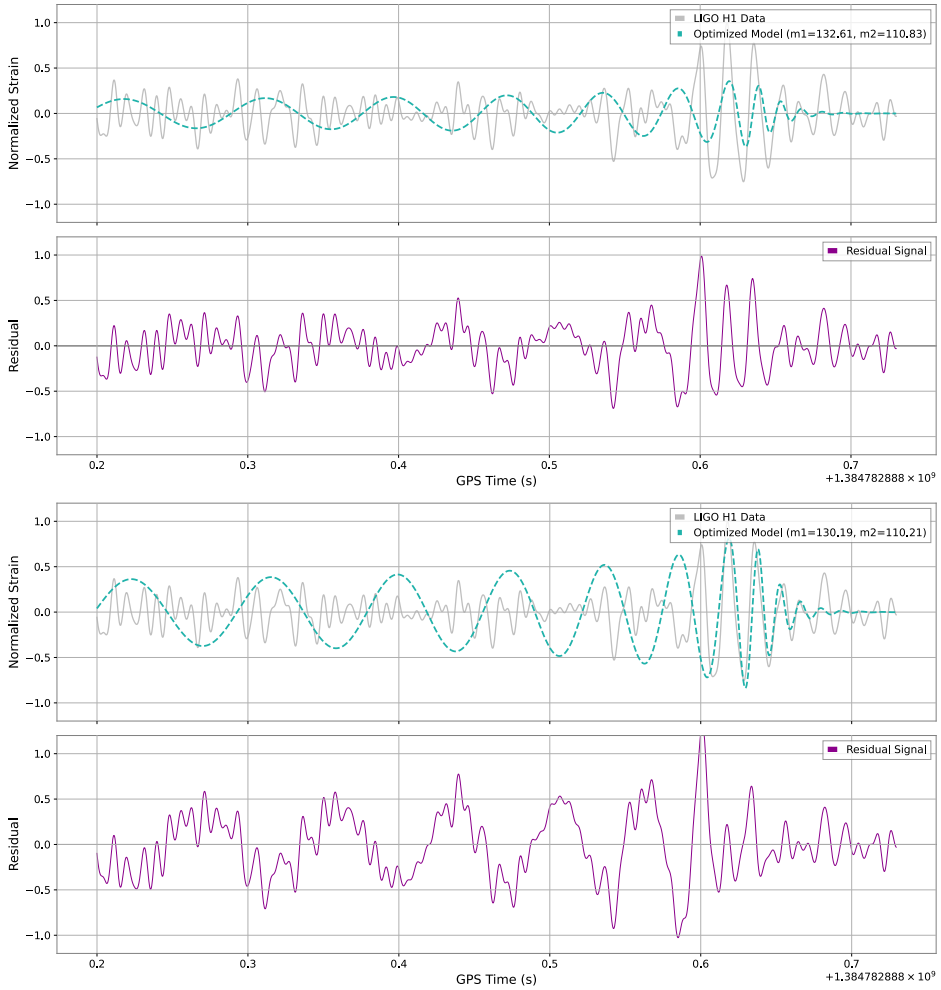

Figure 8.4: *First:* GW231123 data from Hanford (Washington, US) with optimised model focused on the inspiral part of the data; *Second:* Residual signal from modelling GW170814 H1 data with focus on the inspiral part; *Third:* GW231123 data from Hanford (Washington, US) with optimised model focused on the merge part of the data; *Fourth:* Residual signal from modelling GW170814 H1 data with focus on the merger part.

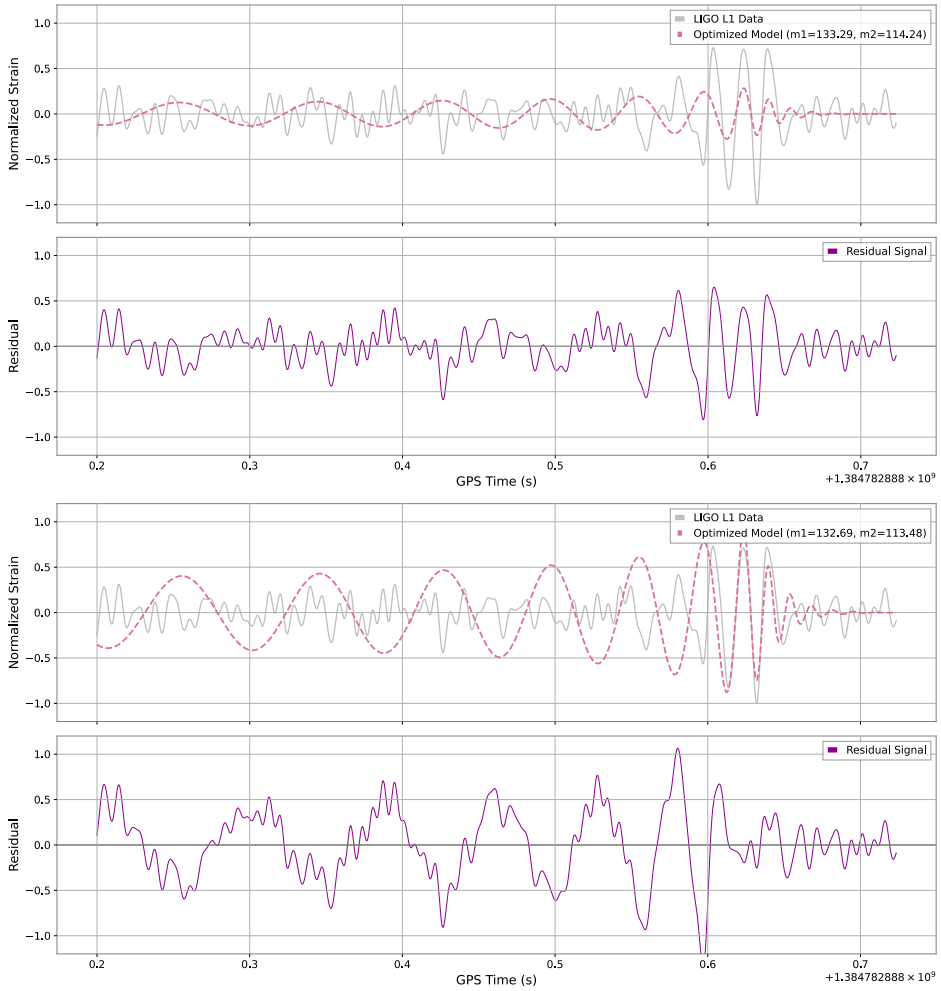

Figure 8.5: *First:* GW231123 data from Livingston (Louisiana, US) with optimised model focused on the inspiral part of the data; *Second:* Residual signal from modelling GW170814 L1 data with focus on the inspiral part; *Third:* GW231123 data from Livingston (Louisiana, US) with optimised model focused on the merge part of the data; *Fourth:* Residual signal from modelling GW170814 L1 data with focus on the merge part.

8.3 Results

Parameters of H1	Inspiral	Merge
Primary mass ($M_\odot$)	132.61	130.19
Secondary mass ($M_\odot$)	110.83	110.21
Chirp Mass ($M_\odot$)	105.45	104.20
Time offset (ns)	1.23	1.17
Scale	-0.37	-0.84
Overlap (%)	16.58	18.03

Table 8.1: Results of the analysis and modelling of the H1 GW231123 data.

Parameters of L1	Inspiral	Merge
Primary mass ($M_\odot$)	133.29	132.69
Secondary mass ($M_\odot$)	114.24	113.48
Chirp Mass ($M_\odot$)	107.36	106.76
Time offset (ns)	-8.60	-8.70
Scale	0.28	0.90
Overlap (%)	15.75	15.56

Table 8.2: Results of the analysis and modelling of the L1 GW231123 data.

9 Overall results of analysis

The objective of this analysis was to obtain the primary and secondary masses, m_1 and m_2 and the chirp mass, $\mathcal{M}_c$. The final results were calculated using the arithmetic mean. The Arithmetic Mean is equal to the summation of n numbers divided by n, so the equation is $\bar{x} = \frac{1}{n}\sum_{i=1}^{n} x_i$. The standard deviation equation, namely $\sigma = \sqrt{\frac{\sum(x-\bar{x})^2}{(n-1)}}$, was calculated for every event except GW170817, as it has only one value for each parameter. The means and deviations were calculated in Excel using the functions **AVERAGE** and **STDEVA**. The final results are written in the Table 9.1.

Parameters	GW150814	GW170814	GW170817	GW231123
m_1 $(M_\odot)$	35.40 ± 0.25	30.85 ± 0.17	1.46	132.20 ± 1.37
m_2 $(M_\odot)$	30.22 ± 0.04	24.97 ± 0.18	1.26	112.19 ± 1.97
$\mathcal{M}_c$ $(M_\odot)$	28.46 ± 0.12	24.14 ± 0.02	1.18	105.94 ± 1.41

Table 9.1: Mean values of the final results of each studied event with deviations

10 Conclusion

The main goal of this thesis was to obtain valuable mass parameters for a selected sample of gravitational-wave events.

In the Theoretical section, the key concepts of gravitational-wave physics were presented. This chapter is structured to guide the reader through the theoretical physics of GWs, beginning with fundamental assumptions, continuing with gauge choices, wave solutions, and polarisation properties, and ending with the energy and momentum in a two-body system.

Following the physical background, the Analytical section introduces the core research. It includes an overview of the Python package, the waveform model, and the optimisation methods used in the analysis. The aim is to give the reader a clear picture of the computational tools and procedures used to obtain the results. Once this overview is established, the main investigations are carried out. For clarity, each chapter focuses on a single event, and the final chapter integrates the findings into an overall conclusion. In every event-specific chapter, subsections on data preparation, modelling, and results are included. The chapter on GW150914 contains additional detail, as it serves as a reference example for the reader. The other chapters are organised to highlight how the analysis strategy is tailored to each event. All chapters feature key figures and tables summarising the results. Section **??**, titled *Overall results of analysis*, presents the calculated mean values of all mass parameters inferred during the analysis.

To comment on the results and evaluate their correctness, the published papers of each event (Abac et al. 2025; B. P. Abbott et al. 2016, 2017a,b) and parameters from GWOSC (R. Abbott et al. 2023; Rich Abbott et al. 2021; Collaboration et al. 2025) are used.

The following widely accepted values have been established for GW150914: $m_1 = 34.6^{+4.4}_{-2.6}\,M_\odot$, $m_2 = 30.0^{+2.9}_{-4.6}\,M_\odot$, and $\mathcal{M}_\mathrm{c} = 27.9^{+1.7}_{-1.5}\,M_\odot$. The results were within the specified deviation interval. The overlap percentage is reasonable given that the model is theoretical and the data, even after cleaning, could contain noise. In certain instances, the residuals may appear more indicative of the data than of mere Gaussian noise. However, this could be attributable to the relatively limited time interval under study. The residuals may appear more like

noise when viewed in the context of the larger data set. The amplitude of the residual is predominantly within the range of -0.5 to 0.5, which aligns with the findings outlined in the paper (B. P. Abbott et al. 2016). Therefore, the analysis was successful.

The mass values for GW170814 are as follows: $m_1 = 30.5^{+5.7}_{-3.0}\,M_\odot$, $m_2 = 30.0^{+2.8}_{-4.2}\,M_\odot$, and $\mathcal{M}_c = 24.1^{+1.4}_{-1.1}\,M_\odot$. The masses are once again within the deviation interval. The overlap between the data and model, which is 43.93% and 55.35%, is not the most optimal result. In many cases, the residuals closely mirror the modelled data, particularly during the ringdown phase. In other places, it is evident that the model demonstrates clear deficiencies in that area. The amplitude of the residuals is also within a wide interval. Despite all the aforementioned points, the fitted data bear a resemblance to Figure 1 in (B. P. Abbott et al. 2017a), which suggests that the error may not be as significant as initially thought. Consequently, this analysis was also successful.

The GW170817 values are as follows: $m_1 = 1.46^{+0.12}_{-0.10}\,M_\odot$, $m_2 = 1.27^{+0.09}_{-0.09}\,M_\odot$, and $\mathcal{M}_c = 1.18^{+0.001}_{-0.001}\,M_\odot$. The values obtained were found to be comparable to the official values. From a visual standpoint, the model does not appear to be a good fit. The residuals bear a resemblance to the data, and the overlap percentage indicates the orthogonality of the vectors. The original paper (B. P. Abbott et al. 2017b) utilised a glitch model exclusively for the Livingston data, as illustrated in Figure 2. This demonstrates that the analysis was conducted with good intent but with incorrect assumptions. The validity of the results of this analysis is due entirely to chance. Consequently, the analysis was labelled invalid.

Finally, the GW231123 mass values are as follows: $m_1 = 133^{+17}_{-12}\,M_\odot$, $m_2 = 110^{+15}_{-15}\,M_\odot$, and $\mathcal{M}_c = 115^{+11.8}_{-8,0}\,M_\odot$. The values obtained are comparable to the official values. The present analysis differed from previous analyses in that it was divided into four modelling sessions. It is evident that the residuals closely mirror the configuration of the inspiral data when the merger is modelled, and vice versa. Unfortunately, the amplitude of the residuals is also elevated at the focused parts. The overlap of $15 - 18\%$ is unsatisfactory, even within the context of divided modelling. In comparison with the data presented in the paper (Abac et al. 2025), the data were modelled in a single step, and the model demonstrated a better visual fit. The accuracy of

the results may be attributable to the substantial deviation interval and the manual adjustment of the intervals. This analysis could be considered partly successful, but there may be some inaccuracies.

To summarise, the research proved to be mostly successful, both visually and parametrically. This method could therefore be optimal for the straightforward acquisition of GW masses within different research contexts, or for the rapid acquisition of information in extensive mass research, especially in the case of stellar-mass BBHM. This opinion is based on the understanding that modelling could take many days or weeks. This approach ensures the accuracy necessary for reliable calculations.

References

Abac, A. G. et al. (Oct. 2025). "GW231123: A Binary Black Hole Merger with Total Mass $190 - 265\,M_\odot$". In: *The Astrophysical Journal Letters* 993.1, p. L25. ISSN: 2041-8213. DOI: 10.3847/2041-8213/ae0c9c. URL: http://dx.doi.org/10.3847/2041-8213/ae0c9c.

Abbott, B. P. et al. (Feb. 2016). "Observation of Gravitational Waves from a Binary Black Hole Merger". In: *Physical Review Letters* 116.6. ISSN: 1079-7114. DOI: 10.1103/physrevlett.116.061102. URL: http://dx.doi.org/10.1103/PhysRevLett.116.061102.

Abbott, B. P. et al. (Oct. 2017a). "GW170814: A Three-Detector Observation of Gravitational Waves from a Binary Black Hole Coalescence". In: *Physical Review Letters* 119.14. ISSN: 1079-7114. DOI: 10.1103/physrevlett.119.141101. URL: http://dx.doi.org/10.1103/PhysRevLett.119.141101.

Abbott, B. P. et al. (Oct. 2017b). "GW170817: Observation of Gravitational Waves from a Binary Neutron Star Inspiral". In: *Phys. Rev. Lett.* 119 (16), p. 161101. DOI: 10.1103/PhysRevLett.119.161101. URL: https://link.aps.org/doi/10.1103/PhysRevLett.119.161101.

Abbott, R. et al. (July 2023). "Open Data from the Third Observing Run of LIGO, Virgo, KAGRA, and GEO". In: *The Astrophysical Journal Supplement Series* 267.2, p. 29. DOI: 10.3847/1538-4365/acdc9f. URL: https://doi.org/10.3847/1538-4365/acdc9f.

Abbott, Rich et al. (2021). "Open data from the first and second observing runs of Advanced LIGO and Advanced Virgo". In: *SoftwareX* 13, p. 100658. ISSN: 2352-7110. DOI: https://doi.org/10.1016/j.softx.2021.100658. URL: https://www.sciencedirect.com/science/article/pii/S2352711021000030.

Bohé, Alejandro et al. (Feb. 2017). "Improved effective-one-body model of spinning, nonprecessing binary black holes for the era of gravitational-wave astrophysics with advanced detectors". In: *Physical Review D* 95.4. ISSN: 2470-0029. DOI: 10.1103/physrevd.95.044028. URL: http://dx.doi.org/10.1103/PhysRevD.95.044028.

Buonanno, A. and T. Damour (Mar. 1999). "Effective one-body approach to general relativistic two-body dynamics". In: *Physical Review D* 59.8. ISSN: 1089-4918. DOI: 10.1103/physrevd.59.084006. URL: http://dx.doi.org/10.1103/PhysRevD.59.084006.

Collaboration, The LIGO Scientific et al. (2025). *Open Data from LIGO, Virgo, and KAGRA through the First Part of the Fourth Observing Run*. arXiv: 2508.18079 [gr-qc]. URL: https://arxiv.org/abs/2508.18079.

Damour, Thibault (Mar. 2008). "INTRODUCTORY LECTURES ON THE EFFECTIVE ONE BODY FORMALISM". In: *International Journal of Modern Physics A* 23.08, pp. 1130–1148. ISSN: 1793-656X. DOI: 10.1142/s0217751x08039992. URL: http://dx.doi.org/10.1142/S0217751X08039992.

Hergetová, Leontýna (2024). *Gravitační vlny: nové okno do vesmíru* [*online*]. Bakalářská práce. URL: https://is.muni.cz/th/mzclx/.

Jones, Eric, Travis Oliphant, Pearu Peterson, et al. (2001–). *SciPy: Open source scientific tools for Python - scipy.optimize. differential$_e$volution*. URL: https://docs.scipy.org/doc/scipy/reference/generated/scipy.optimize.differential_evolution.html.

LIGO Scientific Collaboration, Virgo Collaboration, and KAGRA Collaboration (2018). *LVK Algorithm Library - LALSuite*. Free software (GPL). DOI: 10.7935/GT1W-FZ16.

Maggiore, Michele (2008). *Gravitational Waves: Volume 1: Theory and Experiments*. Oxford University Press.

mykd (2021). *What is a Padé; approximant?* Matter Modeling Stack Exchange. URL:https://mattermodeling.stackexchange.com/q/6552 (version: 2021-08-12). eprint: https://mattermodeling.stackexchange.com/q/6552. URL: https://mattermodeling.stackexchange.com/q/6552.

Nagar, Alessandro et al. (Nov. 2018). "Time-domain effective-one-body gravitational waveforms for coalescing compact binaries with nonprecessing spins, tides, and self-spin effects". In: *Physical Review D* 98.10. ISSN: 2470-0029. DOI: 10.1103/physrevd.98.104052. URL: http://dx.doi.org/10.1103/PhysRevD.98.104052.

Nitz, Alex, Ian Harry, et al. (2024). *PyCBC Tutorials*. https://github.com/gwastro/PyCBC-Tutorials.

Nitz, Alex et al. (Jan. 2024). *gwastro/pycbc: v2.3.3 release of PyCBC*. Version v2.3.3. DOI: 10.5281/zenodo.10473621. URL: https://doi.org/10.5281/zenodo.10473621.

Storn, Rainer and Kenneth Price (Jan. 1997). "Differential Evolution - A Simple and Efficient Heuristic for Global Optimization over

Continuous Spaces". In: *Journal of Global Optimization* 11, pp. 341–359. DOI: 10.1023/A:1008202821328.

Tom Krantz, Alexandra Jonker (2025). *What Is Cosine Similarity? | IBM — ibm.com*. https://www.ibm.com/think/topics/cosine-similarity. [Accessed 11-04-2026].

Virtanen, Pauli et al. (2020). "SciPy 1.0: Fundamental Algorithms for Scientific Computing in Python". In: *Nature Methods* 17, pp. 261–272. DOI: 10.1038/s41592-019-0686-2.

Index

B
BBH, 65
BBHM, 44
BNSM, 41, 60

D
DE, 41

E
EOB, 37

G
GR, 20
GWs, 12

L
LM, 5
LS, 49

P
PDS, 45
PN, 39

R
RC, 43

T
T-M tensor, 10
T-T gauge, 14

A Appendix

A.1 Detailed calculations from chapter "Linear theory in weak field approximation"

This section was created to help understand the steps taken in deriving Section 1 *Linear Theory in Weak Field Approximation*.

A.1.1 Equation of linearised gravity using trace-reversed tensor (1.13)

$$\partial_\rho\partial_\mu\left[\eta^{\rho\mu}\left(\phi_{\mu\nu}-\frac{1}{2}\eta_{\mu\nu}\phi\right)\right]+\partial_\rho\partial_\nu\left[\eta^{\rho\nu}\left(\phi_{\mu\nu}-\frac{1}{2}\eta_{\mu\nu}\phi\right)\right]+ \tag{A.1}$$

$$+\partial_\mu\partial_\nu\phi-\Box\left(\phi_{\mu\nu}-\frac{1}{2}\eta_{\mu\nu}\phi\right)\eta_{\mu\nu}\partial_\rho\partial_\mu\left[\eta^{\mu\nu}\eta^{\mu\rho}\left(\phi_{\mu\nu}-\frac{1}{2}\eta_{\mu\nu}\phi\right)\right]-$$

$$-\eta_{\mu\nu}\Box\phi=\frac{16\pi G}{c^4}T_{\mu\nu}\Rightarrow \tag{A.2}$$

$$\partial_\rho\partial_\mu\phi^\rho{}_\nu-\frac{1}{2}\partial_\mu\partial_\nu\phi+\partial_\rho\partial_\nu\phi^\rho{}_\mu-\frac{1}{2}\partial_\mu\partial_\nu\phi+\partial_\mu\partial_\nu\phi-\Box\phi_{\mu\nu}+$$

$$+\frac{1}{2}\eta_{\mu\nu}\Box\phi-\eta_{\mu\nu}\partial_\rho\partial_\mu\phi^{\mu\rho}+\frac{1}{2}\eta_{\mu\nu}\Box\phi-\eta_{\mu\nu}\Box\phi=\frac{16\pi G}{c^4}T_{\mu\nu}\Rightarrow$$

$$\partial_\rho\partial_\mu\phi^\rho{}_\nu+\partial_\rho\partial_\nu\phi^\rho{}_\mu-\Box\phi_{\mu\nu}-\eta_{\mu\nu}\partial_\rho\partial_\mu\phi^{\mu\rho}=\frac{16\pi G}{c^4}T_{\mu\nu}$$

A.1.2 Derivatives used for coordinate change (1.16)

$$\frac{\partial x^\mu}{\partial x^{\nu\prime}}=\delta^\mu_\nu-\partial'_\nu\xi^\mu=\delta^\mu_\nu-\frac{\partial x^\alpha}{\partial x'^\nu}\frac{\partial\xi^\mu}{\partial x^\alpha}=\delta^\mu_\nu-\left(\delta^\alpha_\nu-\partial'_\nu\xi^\alpha\right)\frac{\partial\xi^\mu}{\partial x^\alpha}\approx\delta^\mu_\nu-\partial_\nu\xi^\mu \tag{A.3}$$

A.1.3 Trace reversed perturbation with gauge condition (1.18)

$$h' = \eta^{\mu\nu} h'_{\mu\nu} = \eta^{\mu\nu}(h_{\mu\nu} - \partial_\mu \xi_\nu - \partial_\nu \xi_\mu) = h^\mu_\mu - \partial_\mu \xi^\mu - \partial_\nu \xi^\nu = h - 2\partial_\alpha \xi^\alpha, \tag{A.4}$$

$$\phi'_{\mu\nu} = h'_{\mu\nu} - \frac{1}{2}\eta_{\mu\nu} h' \Rightarrow$$

$$h_{\mu\nu} - \partial_\mu \xi_\nu - \partial_\nu \xi_\mu - \frac{1}{2}\eta_{\mu\nu}(h - 2\partial_\alpha \xi^\alpha), \quad \phi_{\mu\nu} = h_{\mu\nu} - \frac{1}{2}\eta_{\mu\nu} h \Rightarrow$$

$$\phi'_{\mu\nu} = \phi_{\mu\nu} - \partial_\mu \xi_\nu - \partial_\nu \xi_\mu + \eta_{\mu\nu}\partial_\lambda \xi^\lambda \tag{A.5}$$

A.2 Detailed calculations from chapter "Gravitational waves emitted from a two-body system"

A.2.1 Calculation of the last non-linear term in the second-order Ricci tensor (3.3)

$$\begin{aligned}
-\Gamma^{\rho}_{\mu\lambda}\Gamma^{\lambda}_{\nu\rho} &= -\tfrac{1}{4}\,\eta^{\rho\sigma}\left(\partial_\mu h_{\lambda\sigma} + \partial_\lambda h_{\mu\sigma} - \partial_\sigma h_{\mu\lambda}\right)\eta^{\lambda\sigma}\left(\partial_\nu h_{\rho\sigma} + \partial_\rho h_{\nu\sigma} - \partial_\sigma h_{\nu\rho}\right) \\
&= -\tfrac{1}{4}\left(\partial_\mu h^{\rho}_{\lambda} + \partial_\lambda h^{\rho}_{\mu} - \partial^{\rho} h_{\mu\lambda}\right)\eta^{\lambda\sigma}\left(\partial_\nu h_{\rho\sigma} + \partial_\rho h_{\nu\sigma} - \partial_\sigma h_{\nu\rho}\right) \\
&= -\tfrac{1}{4}\left(\partial_\mu h^{\rho\sigma} + \partial^{\sigma} h^{\rho}_{\mu} - \partial^{\rho} h^{\sigma}_{\mu}\right)\left(\partial_\nu h_{\rho\sigma} + \partial_\rho h_{\nu\sigma} - \partial_\sigma h_{\nu\rho}\right) \\
&= -\tfrac{1}{4}\Big[(\partial_\mu h^{\rho\sigma})(\partial_\nu h_{\rho\sigma}) + (\partial_\mu h^{\rho\sigma})(\partial_\rho h_{\nu\sigma}) - (\partial_\mu h^{\rho\sigma})(\partial_\sigma h_{\nu\rho}) \\
&\quad + (\partial^{\sigma} h^{\rho}_{\mu})(\partial_\nu h_{\rho\sigma}) + (\partial^{\sigma} h^{\rho}_{\mu})(\partial_\rho h_{\nu\sigma}) - (\partial^{\sigma} h^{\rho}_{\mu})(\partial_\sigma h_{\nu\rho}) \\
&\quad - (\partial^{\rho} h^{\sigma}_{\mu})(\partial_\nu h_{\rho\sigma}) - (\partial^{\rho} h^{\sigma}_{\mu})(\partial_\rho h_{\nu\sigma}) + (\partial^{\rho} h^{\sigma}_{\mu})(\partial_\sigma h_{\nu\rho})\Big].
\end{aligned} \tag{A.6}$$

The second term cancels with the third term, and the fourth term cancels with the seventh term due to the obvious symmetry of the metric. Therefore

$$\begin{aligned}
-\Gamma^{\rho}_{\mu\lambda}\Gamma^{\lambda}_{\nu\rho} = -\tfrac{1}{4}\Big[&(\partial_\mu h^{\rho\sigma})(\partial_\nu h_{\rho\sigma}) + (\partial^{\sigma} h^{\rho}_{\mu})(\partial_\rho h_{\nu\sigma}) - (\partial^{\sigma} h^{\rho}_{\mu})(\partial_\sigma h_{\nu\rho}) \\
&- (\partial^{\rho} h^{\sigma}_{\mu})(\partial_\rho h_{\nu\sigma}) + (\partial^{\rho} h^{\sigma}_{\mu})(\partial_\sigma h_{\nu\rho})\Big].
\end{aligned} \tag{A.7}$$

The second and the fifth terms are identical due to the symmetry of indices $\partial^{\sigma} h^{\rho}_{\mu} = \partial^{\rho} h^{\sigma}_{\mu}$ as well as $\partial_\rho h_{\nu\sigma} = \partial_\sigma h_{\nu\rho}$. This also applies to the third and fourth terms. Simplifying the terms gives

$$-\Gamma^{\rho}_{\mu\lambda}\Gamma^{\lambda}_{\nu\rho} = -\frac{1}{4}(\partial_\mu h^{\rho\sigma})(\partial_\nu h_{\rho\sigma}) + \frac{1}{2}(\partial^{\sigma} h^{\rho}_{\mu})(\partial_\rho h_{\nu\sigma}) - \frac{1}{2}(\partial^{\sigma} h^{\rho}_{\mu})(\partial_\sigma h_{\nu\rho}). \tag{A.8}$$

Finally, rewriting the second and third terms on the right-hand side using the rule for the derivative of the product of two functions as

$$\frac{1}{2}(\partial^{\sigma} h^{\rho}_{\mu})(\partial_\rho h_{\nu\sigma}) = \frac{1}{2}\partial^{\sigma}(h^{\rho}_{\mu}\partial_\rho h_{\nu\sigma}) - \frac{1}{2}h^{\rho}_{\mu}\partial_\rho\partial^{\sigma} h_{\nu\sigma}, \tag{A.9}$$

$$-\frac{1}{2}(\partial^{\sigma} h^{\rho}_{\mu})(\partial_\sigma h_{\nu\rho}) = -\frac{1}{2}\partial^{\sigma}(h^{\rho}_{\mu}\partial_\sigma h_{\nu\rho}) + \frac{1}{2}h^{\rho}_{\mu}\partial^{\sigma}\partial_\sigma h_{\nu\rho}, \tag{A.10}$$

where in the first equation the last term vanishes due to the gauge condition $\partial_\rho \phi^{\rho\nu} = 0$.

A.2.2 Verification of tracelessness and transversality of $q^{ij}_{TT} = Q^{ij}_{TT}$

A general property of a projection operator is

$$
\begin{aligned}
P^2 &= P \wedge P_a^{\ b} P_c^{\ a} = P_c^{\ b}, \qquad \text{(A.11)}\\
P^2 &= \left(\delta_a^{\ b} - \frac{x^b x_a}{r^2}\right)\left(\delta_c^{\ a} - \frac{x^a x_c}{r^2}\right)\\
&= \delta_a^{\ b}\delta_c^{\ a} - \delta_a^{\ b}\frac{x^a x_c}{r^2} - \delta_c^{\ a}\frac{x^b x_a}{r^2} + \frac{x^b x_a}{r^2}\frac{x^a x_c}{r^2}\\
&= \delta_c^{\ b} - \frac{x^b x_c}{r^2} - \frac{x^b x_c}{r^2} + \frac{x^b r^2 x_c}{r^4}\\
&= \delta_c^{\ b} - \frac{x^b x_c}{r^2} = P, \quad \text{that is, } P^2 = P.
\end{aligned}
$$

$$
\begin{aligned}
\text{Equivalently,} \quad P^2 &= \left(\delta_a^{\ b} - n^b n_a\right)(\delta_c^{\ a} - n^a n_c) \qquad \text{(A.12)}\\
&= \delta_a^{\ b}\delta_c^{\ a} - \delta_a^{\ b} n^a n_c - \delta_c^{\ a} n^b n_a + n^b n_a n^a n_c\\
&= \delta_c^{\ b} - n^b n_c - n^b n_c + n^b n_c = \delta_c^{\ b} - n^b n_c = P.
\end{aligned}
$$

With this, the verification of the tracelessness and transversality of $q^{ij}_{TT} = Q^{ij}$ can begin.

Transversality: $x \cdot Q^{ij}_{TT} = 0$

$x_i Q^{ij}_{TT} = (x_i P_a^{\ i}) Q_{ab} P_b^{\ j} - \frac{1}{2} P_{ab} Q_{ab} (x_i P^{ij})$, checking in particular that:

$$
\begin{aligned}
x_i P_a^{\ i} &= x_i\left(\delta_a^{\ i} - \frac{x^i x_a}{r^2}\right) = x_a - \frac{x^i x_i}{r^2} x_a = x_a - x_a = 0,\\
n_i P_a^{\ i} &= n_i\left(\delta_a^{\ i} - n^i n_a\right) = n_a - n_i n^i n_a = n_a - n_a = 0,\\
x_i P^{ij} &= x_i\left(\delta^{ij} - \frac{x^i x^j}{r^2}\right) = x^j - \frac{x_i x^i}{r^2} x^j = x^j - x^j = 0,\\
n_i P^{ij} &= n_i\left(\delta^{ij} - n^i n^j\right) = n^j - n_i n^i n^j = n^j - n^j = 0. \qquad \text{(A.13)}
\end{aligned}
$$

Tracelessness: $Q_i^i = 0$

$$
\begin{aligned}
Q_i^i &= g_{ij} Q_{TT}^{ij} = P_a{}^i Q_{ab} P_{ib} - \tfrac{1}{2} P_{ab} Q_{ab} P_i^i, \quad \text{where:} \\
P_a{}^i P_{ib} &= \left(\delta_a{}^i - \frac{x^i x_a}{r^2}\right)\left(\delta_{ib} - \frac{x_i x_b}{r^2}\right) = \delta_{ab} - \frac{x_a x_b}{r^2} = P_{ab}, \\
P_a{}^i P_{ib} &= \left(\delta_a{}^i - n^i n_a\right)\left(\delta_{ib} - n_i n_b\right) = \delta_{ab} - n_a n_b = P_{ab}, \\
\tfrac{1}{2} P_i^i &= \tfrac{1}{2}\left(\delta_i^i - \frac{x^i x_i}{r^2}\right) = \tfrac{1}{2}(3-1) = 1, \quad \text{that is:} \\
\tfrac{1}{2} P_i^i &= \tfrac{1}{2}\left(\delta_i^i - n^i n_i\right) = \tfrac{1}{2}(3-1) = 1, \\
Q_i^i &= P_{ab} Q_{ab} - P_{ab} Q_{ab} = 0.
\end{aligned} \tag{A.14}
$$

A.2.3 Calculation of $\partial t_{\mathrm{ret}} / \partial t$

Firstly, the geometric relation

$$
c(t - t_{\mathrm{ret}}) = R_{\mathrm{ret}} \equiv |\boldsymbol{r}(t) - \boldsymbol{r'}(t_{\mathrm{ret}})| \tag{A.15}
$$

is differentiated over t_{ret} and then, independently, over t, assuming that $\boldsymbol{r}$ is fixed. Differentiating both sides of the identity $R_{\mathrm{ret}}^2 = \boldsymbol{R}_{\mathrm{ret}} \cdot \boldsymbol{R}_{\mathrm{ret}}$ over t_{ret}, gives

$$
2R_{\mathrm{ret}} \frac{\partial R_{\mathrm{ret}}}{\partial t_{\mathrm{ret}}} = 2\boldsymbol{R}_{\mathrm{ret}} \cdot \frac{\partial \boldsymbol{R}_{\mathrm{ret}}}{\partial t_{\mathrm{ret}}}. \tag{A.16}
$$

Regarding the fixed $\boldsymbol{r}$, then $\partial \boldsymbol{R}_{\mathrm{ret}} / \partial t_{\mathrm{ret}} \equiv \partial(\boldsymbol{r} - \boldsymbol{r'}) / \partial t_{\mathrm{ret}} = -\partial \boldsymbol{r'} / \partial t_{\mathrm{ret}} \equiv -\boldsymbol{u}_{\mathrm{ret}}$, then

$$
\frac{\partial R_{\mathrm{ret}}}{\partial t_{\mathrm{ret}}} = \frac{\boldsymbol{R}_{\mathrm{ret}}}{R_{\mathrm{ret}}} \cdot \frac{\partial \boldsymbol{R}_{\mathrm{ret}}}{\partial t_{\mathrm{ret}}} = -\left(\boldsymbol{n} \cdot \boldsymbol{u}\right)_{\mathrm{ret}}. \tag{A.17}
$$

Differentiating in the geometric relation the same R_{ret} over t gives

$$
\frac{\partial R_{\mathrm{ret}}}{\partial t} = c - c \frac{\partial t_{\mathrm{ret}}}{\partial t}, \tag{A.18}
$$

while using the chain rule, the equation is

$$\frac{\partial R_{\text{ret}}}{\partial t} = \frac{\partial R_{\text{ret}}}{\partial t_{\text{ret}}} \frac{\partial t_{\text{ret}}}{\partial t} = -\left(\boldsymbol{n} \cdot \boldsymbol{u}\right)_{\text{ret}} \frac{\partial t_{\text{ret}}}{\partial t}. \tag{A.19}$$

Combining the previous two equations gives

$$\frac{\partial t_{\text{ret}}}{\partial t} = \frac{c}{c - \left(\boldsymbol{n} \cdot \boldsymbol{u}\right)_{\text{ret}}} = \left[\frac{1}{1 - \boldsymbol{\beta} \cdot \boldsymbol{n}}\right]_{\text{ret}}. \tag{A.20}$$

A.2.4 Generalised identities for the solutions of Equation (3.33)

For an odd number of n_i, the integral vanishes because the integrand is odd under parity. In contrast, for an even number of n_i, the tensor $n_{i1}\, n_{i2} \ldots n_{i2k}$ is symmetric. Consequently, its angular integral average can only depend on fully symmetrised products of Kronecker deltas. After fixing the tensor structure, the overall coefficient can be determined by contracting all indices. This leads to the general result

$$\int \frac{\mathrm{d}\Omega}{4\pi}\, n_{i_1}\, n_{i_2} \ldots n_{i_{2k}} = \frac{1}{(2k+1)!!} \left(\delta_{i_1 i_2}\delta_{i_3 i_4} \ldots \delta_{i_{2k-1} i_{2k}} + \ldots\right), \tag{A.21}$$

where !! is a "double factorial" defined as $n(n-2)(n-4)\ldots$. In particular, one obtains

$$\int \frac{\mathrm{d}\Omega}{4\pi} n^a n^b = \frac{1}{3}\eta^{ab}, \tag{A.22}$$

$$\int \frac{\mathrm{d}\Omega}{4\pi} n^a n^b n^c n^d = \frac{1}{15}\left(\eta^{ab}\eta^{cd} + \eta^{ac}\eta^{bd} + \eta^{ad}\eta^{bc}\right), \tag{A.23}$$

which agrees with Eq. (3.33).

A.3 The complete code for the numerical analysis

This code was used for every GW event noted in this thesis. As the final boundaries with bandpass frequencies are written in the main text, there is no need to show the code repeatedly. Please note that this also applies to the code for H1 and L1 analysis. Despite the code being separate for each of them, meaning two codes for every detection, the only difference was the labelling. Still, the changes to the labels can sometimes be confusing, so that part (with the changed labels) will be shown.

A.3.1 The exemplary code for the H1 of GW150914.

```
# IMPORTS
from pycbc.catalog import Merger
import pylab
import numpy as np
from pycbc.waveform import get_td_waveform
from scipy.optimize import differential_evolution
from matplotlib_inline.backend_inline import
    set_matplotlib_formats
from scipy.spatial.distance import cosine

set_matplotlib_formats('svg', 'pdf')


# EVENT
m = Merger('GW150914')

data = {}
for ifo in ['H1', 'L1']:
    data[ifo] = m.strain(ifo)

colors = {'H1': 'lightseagreen', 'L1': 'palevioletred'}
# RAW DATA
for ifo in data:
    pylab.plot(data[ifo].sample_times, data[ifo], label=
    ifo, color=colors[ifo])

pylab.ylabel('Strain')
pylab.xlabel('Time (s)')
pylab.legend()
pylab.show()
```

```
29
30
31 # PSD (POWER SPECTRAL DENSITY)
32 for ifo in data:
33     psd = data[ifo].psd(4)
34     pylab.loglog(psd.sample_frequencies, psd, color=
    colors[ifo],label=ifo)
35
36 pylab.ylabel('$Strain^2 / Hz$')
37 pylab.xlabel('Frequency (Hz)')
38 pylab.grid()
39 pylab.xlim(10, 2048)
40 pylab.legend()
41 pylab.show()
42
43
44 # WHITEN DATA
45 whitened = {}
46
47 for ifo in data:
48     whitened[ifo] = data[ifo].whiten(4, 4)
49     zoom = whitened[ifo].time_slice(m.time - 0.5, m.time
    + 0.5)
50     pylab.plot(zoom.sample_times, zoom, label=ifo, color=
    colors[ifo])
51
52 pylab.ylabel('Whitened Strain')
53 pylab.xlabel('Time (s)')
54 pylab.legend()
55 pylab.show()
56
57
58 # WHITENED PSD
59 pylab.figure(figsize=[10, 5])
60
61 for ifo in whitened:
62     psd_whitened = whitened[ifo].psd(4)
63     pylab.loglog(psd_whitened.sample_frequencies,
    psd_whitened,
64                  label=ifo, color=colors[ifo], alpha=0.8)
65
66 pylab.ylabel('Power Spectral Density (Whitened)')
67 pylab.xlabel('Frequency (Hz)')
68 pylab.grid(True)
69 pylab.xlim(10, 2048)
```

```
pylab.ylim(0.1, 10)
pylab.legend()
pylab.show()


# BANDPASS DATA
for ifo in whitened:
    bpsd = whitened[ifo].highpass_fir(30, 512).lowpass_fir(250, 512)
    zoom = bpsd.time_slice(m.time - 0.5, m.time + 0.5)
    pylab.plot(zoom.sample_times, zoom, label=ifo, color=colors[ifo])

pylab.ylabel('Whitened and Bandpassed Strain')
pylab.xlabel('Time (s)')
pylab.grid()
pylab.legend()
pylab.show()


# MERGER ZOOM
pylab.figure(figsize=[15, 3])

for ifo in whitened:
    bpsd = whitened[ifo].highpass_fir(30, 512).lowpass_fir(250, 512)
    zoom = bpsd.time_slice(m.time - 0.1, m.time + 0.1)
    pylab.plot(zoom.sample_times, zoom, label=ifo, color=colors[ifo])

pylab.ylabel('Whitened and Bandpassed Strain')
pylab.xlabel('Time (s)')
pylab.grid()
pylab.legend()
pylab.show()


# H1 DATA PREP
bps_h1 = whitened['H1'].highpass_fir(30, 512).lowpass_fir(250, 512)
zoom_h1 = bps_h1.time_slice(m.time - 0.1, m.time + 0.05)

data_array = zoom_h1.numpy()
data_array /= np.max(np.abs(data_array))
dt = zoom_h1.delta_t
```

```
110
111
112 # MATCH FUNCTION
113 def match_score(params):
114     m1, m2, time_offset, scale = params
115
116     try:
117         hp, _ = get_td_waveform(
118             approximant="SEOBNRv4",
119             mass1=m1, mass2=m2,
120             delta_t=dt, f_lower=30
121         )
122         model_array = hp.numpy()
123
124         data_peak_idx = np.argmax(np.abs(data_array))
125         model_peak_idx = np.argmax(np.abs(model_array))
126
127         t_gps_peak = zoom_h1.sample_times[data_peak_idx]
128
129         t_shifted_model = (
130             (np.arange(len(model_array)) - model_peak_idx
    ) * dt
131             + t_gps_peak + time_offset
132         )
133
134         model_segment = np.interp(
135             zoom_h1.sample_times,
136             t_shifted_model,
137             model_array,
138             left=0, right=0
139         ) * scale
140
141         if np.max(np.abs(model_segment)) < 1e-5:
142             return 1e12
143
144         return np.sum((data_array - model_segment)**2)
145
146     except:
147         return 1e12
148
149
150 # OPTIMISATION
151 print("Searching for m1 & m2 in H1 beep boop...")
152
153 bounds = [
```

```
    (35.3, 35.7),           #mass1 range
    (30.1, 30.5),           #mass2 range
    (0.0024, 0.0028),   #time offset range
    (0.95, 0.98)            #scale range
]

result = differential_evolution(
    match_score,
    bounds,
    strategy='best1bin',
    popsize=100,
    tol=1e-15
)

best_m1, best_m2, best_time, best_scale = result.x

print(f" Best masses are m1: {best_m1:.2f} and m2: {
    best_m2:.2f} + also time offset: {best_time:.4f} and
    scale: {best_scale:.2f}")

m1_f, m2_f = (best_m1, best_m2) if best_m1 >= best_m2
    else (best_m2, best_m1)


# FINAL MODEL
hp_final, _ = get_td_waveform(
    approximant="SEOBNRv4",
    mass1=m1_f,
    mass2=m2_f,
    delta_t=dt,
    f_lower=30
)

data_times_np = zoom_h1.sample_times.numpy()
model_raw_np = hp_final.numpy()

data_peak_idx = np.argmax(np.abs(data_array))
model_peak_idx = np.argmax(np.abs(model_raw_np))

t_gps_peak = data_times_np[data_peak_idx]

t_shifted_model = (
    (np.arange(len(model_raw_np)) - model_peak_idx) * dt
    + t_gps_peak + best_time
)
```

```
196
197 model_plot = np.interp(
198     data_times_np,
199     t_shifted_model,
200     model_raw_np,
201     left=0, right=0
202 )
203
204 model_plot = (model_plot / np.max(np.abs(model_raw_np)))
    * best_scale
205 data_to_plot = data_array / np.max(np.abs(data_array))
206 residuum = data_to_plot - model_plot
207
208
209 # PLOTING DATA + MODEL + RESIDUAL
210 fig, (ax1, ax2) = pylab.subplots(2, 1, figsize=[15, 8],
    sharex=True)
211
212 if np.max(np.abs(model_plot)) < 0.01:
213     print("\nDEBUG INFO")
214     print(f"Data Time Range: {data_times_np[0]:.2f} to {
    data_times_np[-1]:.2f}")
215     print(f"Model Time Range: {t_shifted_model[0]:.2f} to
     {t_shifted_model[-1]:.2f}")
216     print("------------------\n")
217
218 ax1.plot(data_times_np, data_to_plot, label='LIGO H1 Data
    ', color='gray', alpha=0.5, lw=1.5)
219 ax1.plot(data_times_np, model_plot, label=f'Optimized
    Model (m1={m1_f:.2f}, m2={m2_f:.2f})', color='
    lightseagreen', linestyle='--', lw=2, zorder=5)
220 ax1.set_ylabel("Normalized Strain")
221 ax1.set_ylim(-1.2, 1.2)
222 ax1.legend(loc='upper right')
223 ax1.grid(True)
224
225 ax2.plot(data_times_np, residuum, label='Residual Signal'
    , color='darkmagenta', lw=1)
226 ax2.axhline(0, color='black', lw=1)
227 ax2.set_ylabel('Residual')
228 ax2.set_xlabel("Time (s)")
229 ax2.set_ylim(-1.2, 1.2)
230 ax2.legend(loc='upper right')
231 ax2.grid(True)
232
```

```
pylab.tight_layout()
pylab.show()


#OVERLAP CALCULATION
overlap = np.dot(data_to_plot, model_plot) / (np.linalg.
    norm(data_to_plot) * np.linalg.norm(model_plot))
overlap_percentage = overlap * 100

print(f"Overlap: {overlap_percentage:.2f}%")

# CHIRP MASS CALCULATION
def calculate_chirp_mass(m1, m2):

    numerator = (m1 * m2)**(3/5)
    denominator = (m1 + m2)**(1/5)
    return numerator / denominator

chirp_mass = calculate_chirp_mass(m1_f, m2_f)
print(f"Chirp Mass: {chirp_mass:.2f}")
```

Listing A.1: The complete code for H1 data analysis

A.3.2 The snippet for L1 of GW150914

This snippet is meant to replace the code from `# H1 DATA PREP` to `# OVERLAP CALCULATION`.

```
# L1 DATA PREP
bps_l1 = whitened['L1'].highpass_fir(30, 512).lowpass_fir
    (250, 512)
zoom_l1 = bps_l1.time_slice(m.time - 0.1, m.time + 0.05)

data_array = zoom_l1.numpy()
data_array /= np.max(np.abs(data_array))
dt = zoom_l1.delta_t


# MATCH FUNCTION
def match_score(params):
    m1, m2, time_offset, scale = params
    try:
        hp, _ = get_td_waveform(
            approximant="SEOBNRv4",
            mass1=m1, mass2=m2,
```

```
            delta_t=dt, f_lower=30
        )
        model_array = hp.numpy()

        data_peak_idx = np.argmax(np.abs(data_array))
        model_peak_idx = np.argmax(np.abs(model_array))

        t_gps_peak = zoom_l1.sample_times[data_peak_idx]

        t_shifted_model = (
            (np.arange(len(model_array)) - model_peak_idx
    ) * dt
            + t_gps_peak + time_offset
        )

        model_segment = np.interp(
            zoom_l1.sample_times,
            t_shifted_model,
            model_array,
            left=0, right=0
        ) * scale

        if np.max(np.abs(model_segment)) < 1e-5:
            return 1e12

        return np.sum((data_array - model_segment)**2)

    except:
        return 1e12


# OPTIMISATION
print("Searching for m1 & m2 in L1 beep boop...")

bounds = [
    (35.2, 35.5),       #mass1 range
    (29.9, 30.3),       #mass2 range
    (0.0025, 0.003),  #time offset range
    (-0.88, -0.83)    #scale range
]

result = differential_evolution(
    match_score,
    bounds,
    strategy='best1bin',
```

```
    popsize=100,
    tol=1e-15
)

best_m1, best_m2, best_time, best_scale = result.x

print(f" Best masses are m1: {best_m1:.2f} and m2: {best_m2:.2f} + also time offset: {best_time:.4f} s and scale: {best_scale:.2f}")

m1_f, m2_f = (best_m1, best_m2) if best_m1 >= best_m2 else (best_m2, best_m1)


# FINAL MODEL
hp_final, _ = get_td_waveform(
    approximant="SEOBNRv4",
    mass1=m1_f,
    mass2=m2_f,
    delta_t=dt,
    f_lower=30
)

data_times_np = zoom_l1.sample_times.numpy()
model_raw_np = hp_final.numpy()

data_peak_idx = np.argmax(np.abs(data_array))
model_peak_idx = np.argmax(np.abs(model_raw_np))

t_gps_peak = data_times_np[data_peak_idx]

t_shifted_model = (
    (np.arange(len(model_raw_np)) - model_peak_idx) * dt
    + t_gps_peak + best_time
)

model_plot = np.interp(
    data_times_np,
    t_shifted_model,
    model_raw_np,
    left=0, right=0
)

model_plot = (model_plot / np.max(np.abs(model_raw_np))) * best_scale
```

```
data_to_plot = data_array / np.max(np.abs(data_array))
residuum = data_to_plot - model_plot


# PLOTING DATA + MODEL + RESIDUAL
fig, (ax1, ax2) = pylab.subplots(2, 1, figsize=[15, 8],
    sharex=True)

if np.max(np.abs(model_plot)) < 0.01:
    print("\nDEBUG INFO")
    print(f"Data Time Range: {data_times_np[0]:.2f} to {
    data_times_np[-1]:.2f}")
    print(f"Model Time Range: {t_shifted_model[0]:.2f} to
    {t_shifted_model[-1]:.2f}")
    print("------------------\n")

ax1.plot(data_times_np, data_to_plot, label='LIGO L1 Data
    ', color='gray', alpha=0.5, lw=1.5)
ax1.plot(data_times_np, model_plot, label=f'Optimized
    Model (m1={m1_f:.2f}, m2={m2_f:.2f})', color='
    palevioletred', linestyle='--', lw=2, zorder=5)
ax1.set_ylabel("Normalized Strain")
ax1.set_ylim(-1.2, 1.2)
ax1.legend(loc='upper right')
ax1.grid(True)

ax2.plot(data_times_np, residuum, label='Residual Signal'
    , color='darkmagenta', lw=1)
ax2.axhline(0, color='black', lw=1)
ax2.set_ylabel('Residual')
ax2.set_xlabel("Time (s)")
ax2.set_ylim(-1.2, 1.2)
ax2.legend(loc='upper right')
ax2.grid(True)

pylab.tight_layout()
pylab.show()
```

Listing A.2: The snippet of code used for L1 detector